Coarse-grained modelling for soft matter scattering

submitted by

Andrew R. McCluskey

for the degree of Doctor of Philosophy

of the

UNIVERSITY OF BATH

Department of Chemistry

December, 2018

Declaration of Authorship

I, Andrew R. McCluskey, declare that this thesis titled, "Coarse-grained modelling for soft matter scattering" and the work presented in it are my own. I confirm that:

- where the thesis or any part of the thesis such as a published paper, has been produced jointly with others, that a substantial part is the original work of myself, and

- where the thesis incorporates material already submitted for another degree, the extent of that material and the degree, if any, obtained.

Signed:

———————————————————————

Date:

———————————————————————

"Atticus told me to delete the adjectives and I'd have the facts."

Scout Finch – To Kill a Mockingbird

UNIVERSITY OF BATH

Abstract

Department of Chemistry

Doctor of Philosophy

Coarse-grained modelling for soft matter scattering

by Andrew R. McCluskey

The abstract will go here. This will be a brief description of the work in the thesis.

Acknowledgements

This is where I will acknowledge people. Need to remember everyone...

Reproducibility Statement

This thesis exists as a piece of completely reproducible research. I have endevoured to include as much algorithmic and methodological detail within the text. However, in order to provide complete, and easily, reproducibility an electronic supplementary information (ESI) is available online in the form of a Git repository. This ESI provides full details of the analyses performed in this work and access to an automated analysis workflow.

The ESI may be accessed at the following DOI: 10.5281/zenodo.xxxxxxx.

Contents

List of Abbreviations

BM	bending magnet
DLS	Diamond Light Source
ESRF	European Synchrotron Radiation Facility
ESS	European Spallation Source
GiSAS	grazing incidence small angle scattering
ID	insertion device
ILL	Institut Laue-Langevin
SAS	small angle scattering
ToF	time-of-flight

Physical Constants

$$\pi = 3.1415\dots$$

Planck constant $\quad h = 6.626 \dots \times 10^{-34}\,\mathrm{J\,s}$

List of Symbols

a_0	optimum head-group area	m^2
b	scattering length	m
m	mass	kg
n_i	refractive index	
n	number of individual q-vectors	
q	scattering vector magnitude	m^{-1}
$r_{n,n+1}$	Fresnel equation coefficient	
$res(q)$	resolution function	
t_F	time of flight	s
v	velocity	m s^{-1}
B	resultant matrix	
E_k	kinetic energy	J
I	intensity	
L_F	distance of flight	m
M	layer matrix	
N	number of particles	
N_P	number of magnets	
R	reflected intensity	
S	nuclear spin	
V	volume	m^3
$\mathbf{k}_i$	incident wavevector	m^{-1}
$\mathbf{k}_f$	final wavevector	m^{-1}
$\mathbf{q}$	scattering vector	m^{-1}
$\mathbf{r}_i$	particle position	
β_c	fraction of the speed of light	
β_n	phase factor	
θ	scattering angle	rad
θ_c	critical angle	rad
θ_e	angle between electron and photon	rad
λ	wavelength	m
ρ	scattering lenght density	m^{-2}
σ	interfacial roughness	m
σ_{coh}	coherent cross-section	m^2
σ_{incoh}	incoherent cross-section	m^2
ϕ	scattering angle	rad
ω	frequency	s^{-1}
ω_i	initial frequency	s^{-1}
ω_f	final frequency	s^{-1}
Λ	temperature factor	
Φ	Golden ratio	
$\mathrm{d}\sigma(q)/\mathrm{d}\Omega$	differential cross-section	

1 Introduction

2 Theory

2.1 Scattering

The use of scattering techniques to probe soft condensed matter systems is commonplace. In this work, we have focussed on the use of small angle scattering (SAS), reflectometry, and grazing incidence small angle scattering (GiSAS) techniques. These are particularly appropriate for application to soft condensed matter systems due to the length scales capable of being probed being similar to the persistence length of the soft condensed matter systems. The length scales covered for such techniques is from around $1\,\mathrm{nm}$ to $100\,\mathrm{nm}$, as is shown in Fig. 2.1. Since it is the equilibrium structures(s) under study, there is no interest in the system dynamics. Therefore, the system can be studied using exclusively elastic scattering techniques, where there is no energy transfer between the probing radiation and the system. This is in contrast to inelastic scattering where energy transfer occurs; facilitating the measurement of system dynamics, such as the dynamical modes of polymers of lipid bilayers [1, 2]. The techniques mentioned above all involve the use of elastic scattering and therefore probe the system equilibrium structure.

Both X-ray and neutron scattering techniques are discussed and used in this work. From an experimental viewpoint, there are significant differences between an X-ray scattering and a neutron scattering experiment. However, there is little variation in terms of the data analysis, where the differences are limited to; the nature of the scattering lengths, and the higher background that is present in the neutron scattering experiments.

2.1.1 The scattering vector

The scattering of some probing radiation, by some sample can be represented as shown in Fig. 2.2. Since only elastic scattering is being considered, there will be no change in the frequency of the radiation, $\omega_i = \omega_f$. This means that only the wavevector, $\mathbf{k}$, can change, $\mathbf{k}_i \neq \mathbf{k}_f$. The difference between the incident and final wavevectors is the scattering vector, $\mathbf{q}$, where,

$$\mathbf{q} = \mathbf{k}_i - \mathbf{k}_f. \tag{2.1}$$

The scattering vector strictly has units of m^{-1}, however it is often more practical to use nm^{-1} or $\mathrm{\mathring{A}}^{-1}$. Throughout this work, units of reciprocal Ångstrom will be wherever possible. Since the frequency of the probing radiation does not change during an elastic scattering event, the wavelength, λ, will also not change, meaning that the moduli of the incident and final wavevectors are,

$$|\mathbf{k}_i| = |\mathbf{k}_f| = \frac{2\pi}{\lambda}. \tag{2.2}$$

This means that only the angle will change during the elastic scattering event. The vector diagram in Fig. 2.3 can be used to describe the geometry of an elastic scattering event. From this, and Eqn. 2.2, the value of q, where $q = |\mathbf{q}|$ can be shown as,

$$q = \frac{4\pi \sin\theta}{\lambda}. \tag{2.3}$$

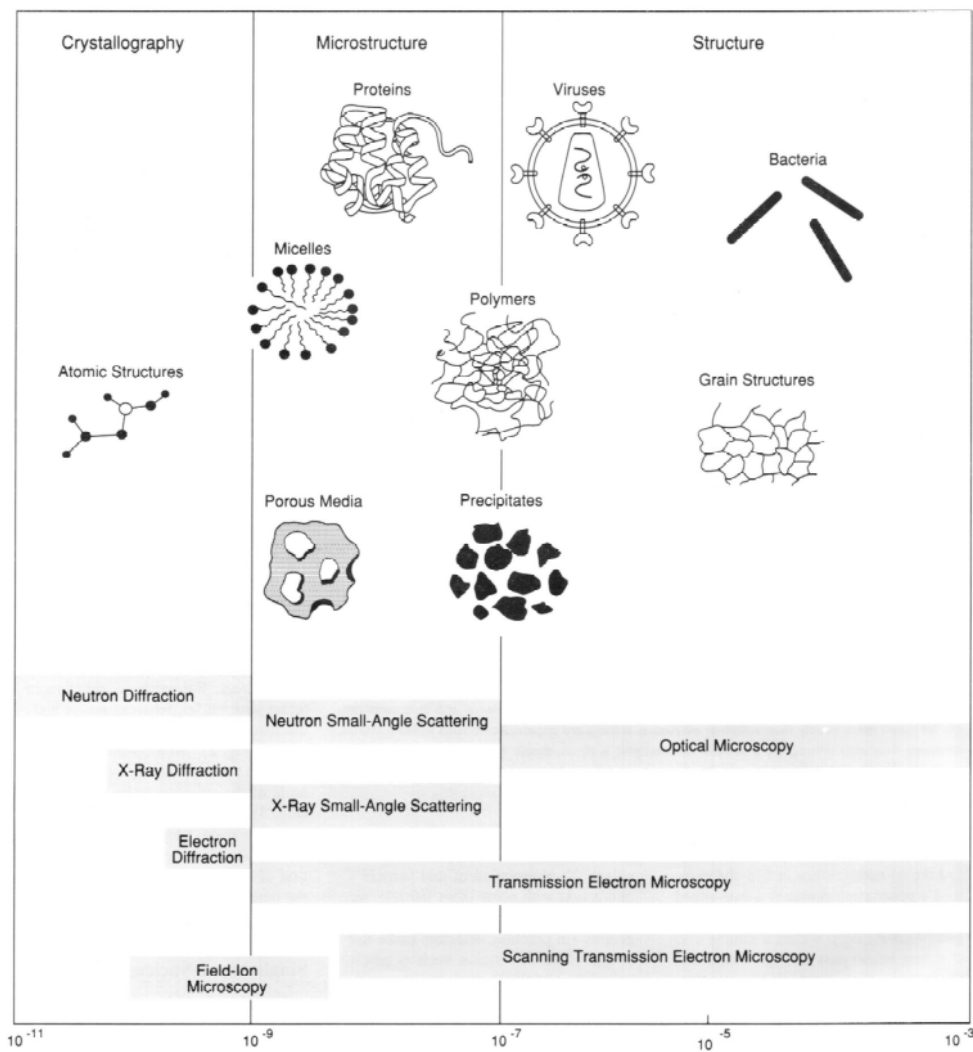However, this fails to fully capture the three dimensional nature of the scattering event.

FIGURE 2.1: A representation of how different techniques can be used to probe various length scales. Reproduced, with permission of Oxford University Press©, from Ref. [3].
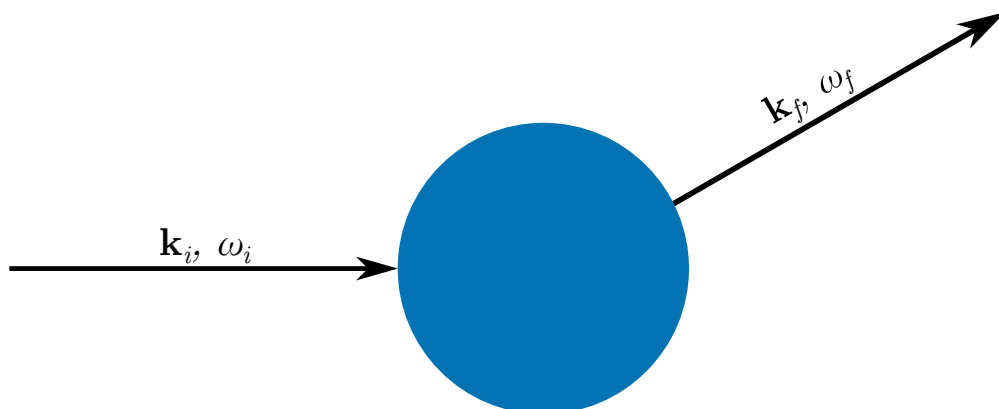

FIGURE 2.2: A schematic of the scattering of some probing radiation by a sample (blue circle). Adapted, with permission of Oxford University Press©, from Ref. [3].
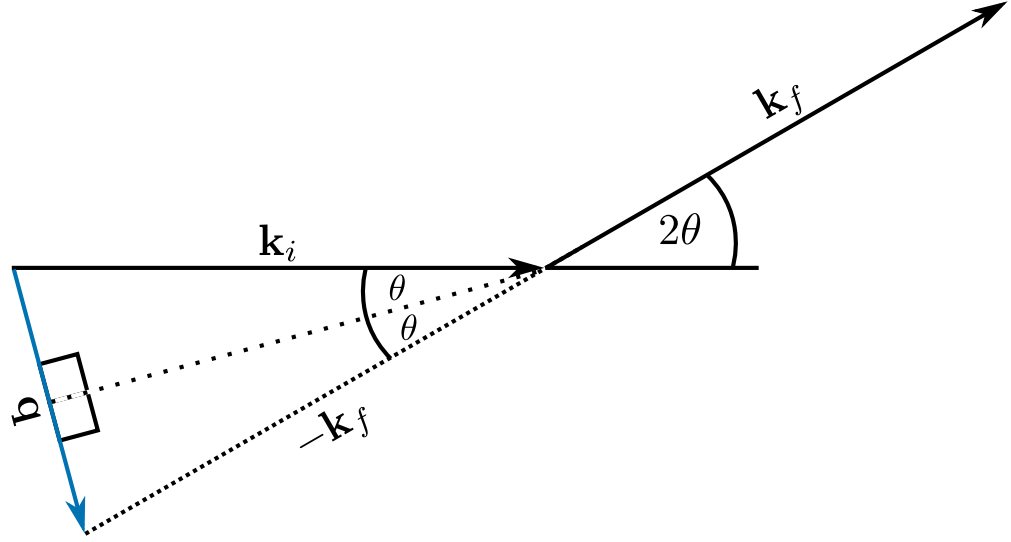
FIGURE 2.3: A vector diagram describing an elastic scattering event. Adapted, with permission of Oxford University Press©, from Ref. [3].

Hence, it is necessary to describe the scattering with spherical coordinates, 2θ, and ϕ, such that the incoming and outgoing radiation can be described as,

$$\mathbf{k}_i = \left(0, 0, \frac{2\pi}{\lambda}\right),$$
$$\mathbf{k}_f = \frac{2\pi}{\lambda}(\sin 2\theta \cos \phi, \sin 2\theta \sin \phi, \cos 2\theta), \tag{2.4}$$

where, $|\mathbf{k}_f| = {2\pi}/{\lambda}$. This allows the scattering vector to be written,

$$\mathbf{q} = \frac{4\pi \sin \theta}{\lambda}(-\cos \theta \cos \phi, -\cos \theta \sin \phi, \sin \theta). \tag{2.5}$$

For an isotropic scattering pattern, it is the magnitude of the scattering vector, q, that is measured. In partical terms, the scattering vector allows for easy comparison of measurements made at different radiation wavelengths.

The basic quantity measured in a scattering experiment is the differential cross section, ${d\sigma(q)}/{d\Omega}$. This is the fraction of particles of probing radiation that are scattered with a particular set of polar coordinates, 2θ and ϕ,

$$\frac{d\sigma(q)}{d\Omega} = \frac{R(2\theta, \phi)}{NV\Phi\Delta\Omega}, \tag{2.6}$$

where, $R(2\theta, \phi)$ is the rate of arrival of the scattered particles at the position 2θ, ϕ, V is the volume of the sample, Φ is incident flux, $\Delta\Omega$ is some small solid angle, and N is the number of scattering particles of interest, in the case of elastically scattering particles, $N = N\%_{\text{el}}$, where $\%_{\text{el}}$ is the fraction of elastically scattered particles.

2.1.2 Scattering from a single fixed particle

It is possible to describe a steady stream of particles of wavelength, λ, travelling through space as follows,

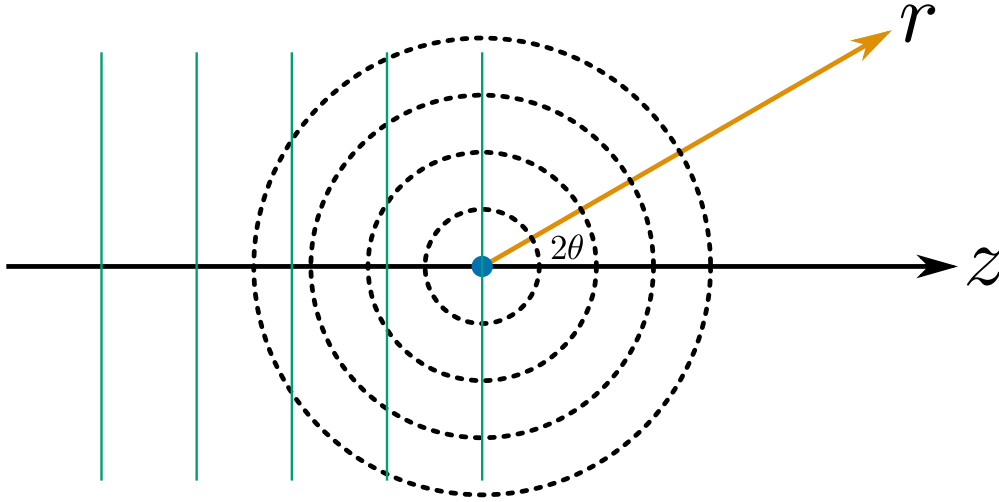$$\psi_i = \psi_o \exp{(\mathbf{i}kz)}, \tag{2.7}$$

FIGURE 2.4: A schematic of the interaction between a single particle and a wave of probing radiation (green lines). Adapted, with permission of Oxford University Press$^{©}$, from Ref. [3].

where, z is the direction of travel, and the incident flux is the magnitude of the wave squared, $\Phi = |\psi_o|^2$. This wave then interacts with a single fixed particle elastically, propagating the wave radially outwards (Fig. 2.4). This propagation is centred on the atom, therefore the wavevector, $\mathbf{k_f}$ is parallel to the displacement vector, $\mathbf{r}$, and the following holds,

$$\exp\left(\mathbf{i}\mathbf{k}_f \cdot \mathbf{r}\right) = \exp\left(\mathbf{i}kr\right). \tag{2.8}$$

This final wave is no longer collimated and therefore deminishes with distance, r. Hence the final scattered wave has the form,

$$\psi_f = \psi_o b \frac{\exp\left(\mathbf{i}kr\right)}{r}, \tag{2.9}$$

where, b is the scattering length discussed in Section 2.2.3.

2.1.3   Scattering from multiple particles

It is important to consider how the probing radiation would interact with a real system, consisting of many particles. If the incident beam has the form of Eqn. 2.7, with the wavevector $\mathbf{k}_i = (0, 0, k)$, each particle, j, will contribute the following to the total scattered wave, psi_f, made up of the scattering from all, N, atoms,

$$[\delta\psi_f]_j = \psi_o \exp\left(\mathbf{i}\mathbf{k}_i \cdot \mathbf{R}_j\right) b_j \frac{\exp\left\{\mathbf{i}\mathbf{k}_f \cdot (\mathbf{r} - \mathbf{R}_j)\right\}}{|\mathbf{r} - \mathbf{R}_j|}, \tag{2.10}$$

where, $\mathbf{R}_j$ is the position of particle j, $\mathbf{r}$ is some arbitrary position, and $\mathbf{k}_f$ is the wavevector of the scattered wave (Fig. 2.5). This allows the total scattered wave to be defined as a summation of the contributions from the individual waves,

$$\psi_f = \psi_o \exp\left(\mathbf{i}\mathbf{k}_f \cdot \mathbf{r}\right) \sum_{j=1}^{N} \left\{ b_j \frac{\exp\left(\mathbf{i}\mathbf{q} \cdot \mathbf{R}_j\right)}{|\mathbf{r} - \mathbf{R}_j|} \right\}. \tag{2.11}$$

Eqn. 2.11 holds true, within the Born approximation, where the scattered wave has no impact on the incident wave and each wave is scattered only once.
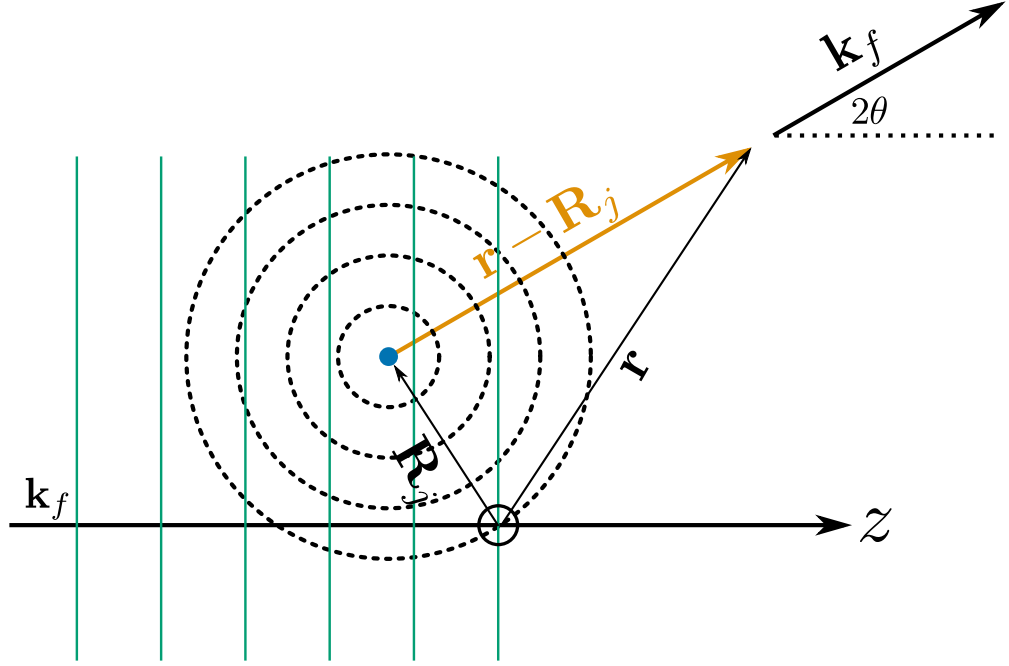
FIGURE 2.5: A schematic of the interaction between a particle, j, at position $\mathbf{R}_j$ and a wave of probing radiation (green lines). Adapted, with permission of Oxford University Press©, from Ref. [3].

The sample-detector distance is usually much larger than the typical particle size, allowing for the following approximation,

$$|\mathbf{r} - \mathbf{R}_j| = |\mathbf{r}| = r. \tag{2.12}$$

This is termed the Fraunhofer, or far-field limit, and allows Eqn. 2.11 to be simplified,

$$|\psi_f|^2 = \frac{\Phi}{r^2} \left| \sum_{j=1}^{N} b_j \exp\left(\mathbf{iq} \cdot \mathbf{R}_j\right) \right|^2. \tag{2.13}$$

In the scattering experiment, particles are deflected elastically into a detector with a small area, δA, with the polar coordinates, 2θ and ϕ, at a rate of R_{el},

$$R_{el}(2\theta, \phi) = |\psi_f|^2 \delta A = \Phi \delta\Omega \left| \sum_{j=1}^{N} b_j \exp\left(\mathbf{iq} \cdot \mathbf{R}_j\right) \right|^2, \tag{2.14}$$

where, $\delta\Omega = \delta A / r^2$. Therefore, the differential cross section, defined in Eqn. 2.6 can be related to the scattering from the sample as,

$$\left(\frac{\mathrm{d}\sigma(q)}{\mathrm{d}\Omega} \right)_{el} = \frac{1}{V} \left| \sum_{j=1}^{N} b_j \exp\left(\mathbf{iq} \cdot \mathbf{R}_j\right) \right|^2. \tag{2.15}$$

2.1.4   Scattering length density

While it may be helpful to consider the scattering of multiple particles individually, where each particle has a scattering length, b. In practice, it is more common to consider the scattering length density, ρ, of the system,

$$\rho = \frac{1}{V} \sum_{i=0}^{N} b_i, \tag{2.16}$$

where N is the total number of particles in the volume V. A result of this equation is the ability to rewrite Eqn. 2.15 as,

$$\left(\frac{\mathrm{d}\sigma(q)}{\mathrm{d}\Omega}\right)_{\mathrm{el}} = \frac{1}{V}\left|\iiint_V \rho \exp\left(\mathbf{iq}\cdot\mathbf{R}\right)\mathrm{d}^3\mathbf{R}\right|^2. \tag{2.17}$$

This above equation shows that the scattering differential cross-section from some object is related to the scattering length density profile of that object by a Fourier transform.

2.1.5   Model-dependent analysis

All types of scattering patterns can be analysed by one of two methods; model independent and model-dependent. The nature of this work means that it will focus on model-dependent analysis methods, often where the model is derived from some atomistic, or coarse-grained simulation. Model-dependent analysis, has significant benefits over model-independent methods, such as improved resolution and more detailed information of the structure. However, the necessisty of the inclusion of *a priori* information within model-dependent analysis may act to bias the result, while this is undesirable, these assumptions can, and should, be educated based on the chemical information present, such as the propensity for twin-tailed lipid molecules to for monolayers at an air-water interface [4].

The scattering from the model system is determined, using technique specific methods that are discuess in detail in laeter sections. This is then compared with the experimental data using some goodness-of-fit metric, as this the model is varied the quality of the fit, and therefore the value of the metric, will improve. In order to accurately reproduce the experimental measurement, it is necessary to include some instrumental resolution function, $res(q)$, in the modelling procedure. This is instrument specific, although it may be approximated by convolving the experimental dataset with some Gaussian smearing function, the modelled intensity can then be determined from,

$$I(q) = res(q) * \frac{\mathrm{d}\sigma(q)}{\mathrm{d}\Omega}, \tag{2.18}$$

where, $\mathrm{d}\sigma(q)/\mathrm{d}\Omega$ is the differential cross-section, a measure of the number of scattering particles hitting a given solid angle of the detector.

The aim of model-dependent analysis is to obtain a model for the system which agrees will with the experimentally measured scattering data, while producing something that is chemically, and physically relevant. This means that optimisation algorithm are often applied to these analysis problems, which are discussed, in detail, in Section 2.5.

2.1.6   Reflectometry

Reflectometry involves the interaction of the probing radiation with some interface, from which the radiation is reflected. The geometry of a reflectometry experiment is shown in
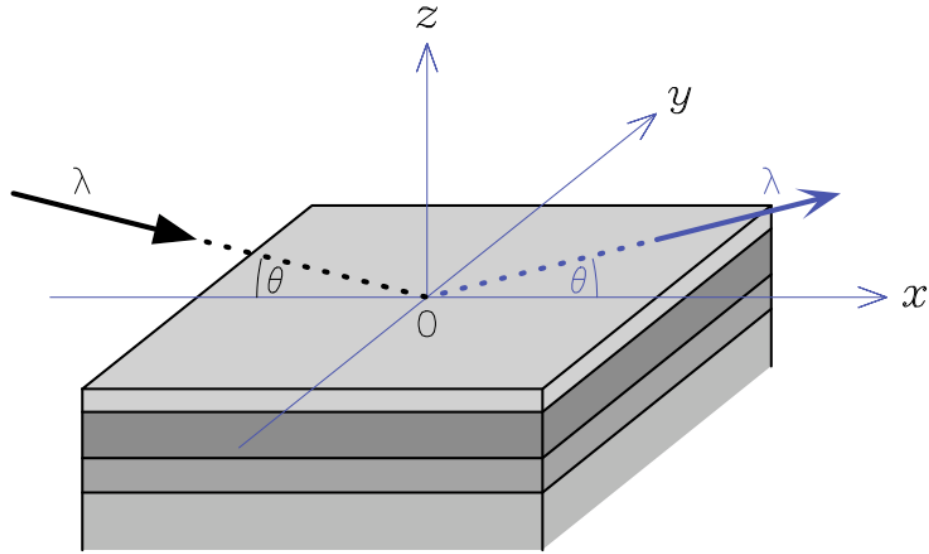
FIGURE 2.6: A schematic of specular reflectometry from a layered sample.
Reproduced, with permission of Oxford University Press©, from Ref. [3].

Fig. 2.6, where the reflectometry instrument is in the horizontal configuration, ideal for the study of liquid interfaces. Reflectometry measurements give information about the structure perpendicular to the interface, the z-dimension in Fig. 2.6, and therefore the analysis of refllectometry data is founding on the assumption that the layers will be completely homogenous in the plane of the interface, the xy-plane in Fig. 2.6. In reality, since the layers are usually not completely homogeneous, an average is obtained for the area in the radiation beam. A reflectometry instrument operates by measuring the intensity of specular radiation at a series of different angles, θ, or wavelengths, λ. The reflected intensity is defined in terms of q (by Eqn. 2.3), and is defined as follows,

$$R(q) = \frac{\text{rate of specular reflective scattering}}{\text{rate of incidence}}.$$ (2.19)

It is clear from Eqn. 2.19 that the value of the measured reflectometry cannot be greater than one, as this would mean that more particles of probing radiation were being reflected than were incident.

Analysis

There are two model-dependent analysis techniques that can be applied to the rationalisation of a reflectometry dataset. The first is the kinematic approach, which can be obtained from Eqn. 2.15, from the assumption that $q_x = 0$ and $q_y = 0$, as we are only measuring the specular scattering. This approach models the reflectometry as a function of the scattering length density profile in the z-dimension, $\rho(z)$,

$$R(q) \approx \frac{16\pi^2}{q^4} \left| \int_{-\infty}^{+\infty} \frac{\mathrm{d}\rho(z)}{\mathrm{d}z} \exp\left(-\mathbf{i}zq_z\right)\mathrm{d}z \right|^2,$$ (2.20)

where, $\mathrm{d}\rho(z)/\mathrm{d}z$ is the first derivative of the scattering length density profile. However, this method has a significant problem, which can be described by applying Eqn. 2.20 to the

scatteirng length density profile of a bare silicon substrate, which can be modelled as a Heaviside function (Fig. 2.7a),

$$\rho(z) = \begin{cases} 0, & \text{if } z < 0 \\ \rho_{Si}, & \text{otherwise} \end{cases} \tag{2.21}$$

where, ρ_{Si} is the scattering length denisty of pure silicon ($2.1 \times 10^{-6}\,\text{Å}^{-2}$ for neutrons). The derivated of a stepwise Heaviside function is a scaled δ-function (Fig. 2.7b),

$$\rho'(z) = \rho_{Si}\delta(z). \tag{2.22}$$

Then, as in Eqn. 2.20, the Fourier transform of this δ-function is taken,

$$\rho_{Si} \int_{-\infty}^{+\infty} \delta(z) \exp\left(-\mathbf{i}zq_z\right)\mathrm{d}z = \rho_{Si} \exp(0) = \rho_{Si}. \tag{2.23}$$

This means that the reflectometry profile could be calculated from the following relationship,

$$R(q) \approx \frac{16\pi^2\rho_{Si}^2}{q_z^4}. \tag{2.24}$$

The curve from this relationship is shown in Fig. 2.7, where it is clear that the agreement with an experimental profile would be poor as $q \to 0$. It can be seen that for low values of q the calculated reflectometry is greater than 1, which violates the physical constraint imposed with Eqn. 2.19. This break down of the kinematic approach is due to the assumption present in this approach that the Born approximation (mentioned in Section 2.1.3) will hold. However, in the reflectometry scattering geometry, this is no longer true rendering the kinematic approach invalid.

This breakdown of the kinematic approach has lead to the application of the Abelès, or Parratt, model for the reflection of light at a given number of stratified inferfaces (also known as dynamical theory) [5, 6]. This methods involves considering the system as a layered structure at the interfaces of which the probing radiation can either be reflected or refracted, by some refractive index, n_i. Fig. 2.8 shows this process for a system of two layers, where the layer 0 is the air or vacuum above the sample, it is clear to see how the two waves labelled r could interfere constructively or destructively depending on the thickness of layer 1, d. This means that for a single interface, suhc as that between layers 0 and 1 in Fig. 2.8, the reflectometry can be described by the Fresnel equation,

$$R(q) = \left| \frac{n_0 \sin\theta_0 - n_1 \sin\theta_1}{n_0 \sin\theta_0 + n_1 \sin\theta_1} \right|^2. \tag{2.25}$$

Additionally at the point of total reflection, where $\theta_0 = \theta_c$, the critical angle, there will be no transmitted wave so,

$$n_1 \sin\theta_1 = 0, \tag{2.26}$$

and therefore the reflected radiation will never be greater than 1, while the critical angle can be defined as,

$$\cos^2\theta_c = \frac{n_1^2}{n_0^2}. \tag{2.27}$$

This is the angle below which a reflectometry profile will be measured.

The above method can then be generalised to a structure of an arbitrary number of layers, as shown in Code Block 2.1. For each value of q for which the reflectometry is to be
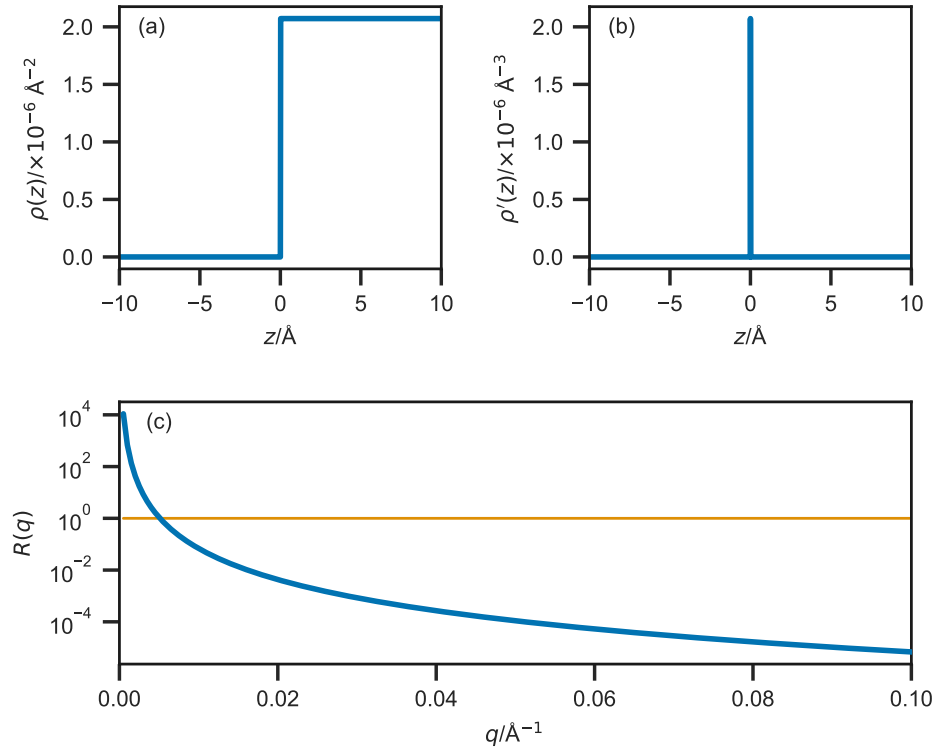
FIGURE 2.7: A graphical representation of the kinematic approach; (a) the Heaviside function describing the scattering length density profile of a bare silicon substrate, (b) the δ-function arising from the first derivative of the function in (a), and (c) the reflectometry profile resulting from Eqn. 2.20, where the orange line at $R = 1$ identifies the break down between experimental and theory in the kinematic approach. Adapted, with permission of Oxford University Press©, from Ref. [3].
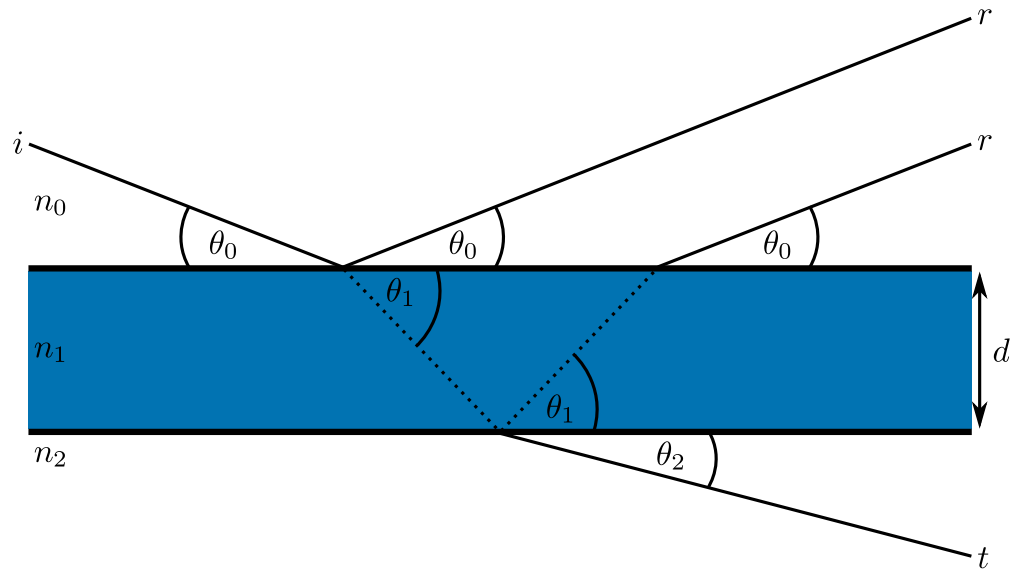

FIGURE 2.8: A schematic diagram showing the reflected (r) and transmitted (t) waves when an incident (i) wave enters an interface of thickness d, where the refractive indices of each layer are n_0, n_1, and n_2. Adapted from [7], with permission from Elsevier.

calculated, the system is considered in terms of $n_{\max}$ layers. The incident radiation beam will be refracted by each of the layers, giving wavevectors values for each layer, k_n,

$$k_n = \sqrt{k_0^2 + 4\pi(\rho_n - \rho_0)}, \tag{2.28}$$

where, $k_0 = q/2$. The Fresnel equation coefficient between layers n and $n+1$, $r_{n,n+1}$ can then be found along with the phase factor, β_n, which is dependent on the thickness of the layer, d_n,

$$r_{n,n+1} = \frac{k_n - k_{n+1}}{k_n + k_{n+1}}, \tag{2.29}$$

$$\beta_n = k_n d_n. \tag{2.30}$$

The means that a matrix can be evaluated for each layer, M_n,

$$M_n = \begin{bmatrix} \exp\beta_n & r_{n,n+1}\exp-\beta_n \\ r_{n,n+1}\exp\beta_n & \exp-\beta_n \end{bmatrix} \tag{2.31}$$

The resultant matrix, B_n, is then found as a product of the matrix from each layer,

$$B = \prod_{n=0}^{n_{\max}} M_n, \tag{2.32}$$

and from this the reflected intensity at the given value of q can be found,

$$R(q_z) = \frac{B_{1,2}}{B_{1,1}}. \tag{2.33}$$

This algorithm models the layers as perfectly flat layers, which will not be strictly true in the case of soft matter systems such as a bilayer. This resulted in the correction term being added to Eqn. 2.29 to account for the roughness of the layers. This adapts Eqn. 2.29 to the form,

$$r_{n,n+1} = \frac{k_n - k_{n+1}}{k_n + k_{n+1}} \exp\left(-2k_n k_{n+1}\sigma_{n,n+1}^2\right), \tag{2.34}$$

where, $\sigma_{n,n+1}$ is the interfacial roughness between layers n and $n+1$. This has the effect of Gaussian broadening the layers into each other, as a result. Code Block 2.1 is currently implemented in a variety of reflectometry modelling software packages, such as refnx, MOTOFIT, RasCAL, and Aurore [8–12]. Applying this method to the scattering length density profile shown in Fig. 2.7 gives the reflectometry profile shown with the dashed green line in Fig. 2.9.

2.1.7   Small angle scattering

Eqn. 2.17 identified that the scattering differential cross-section for some object was related to the scattering length density by a Fourier transform, which is shown graphically in Fig. 2.10. This figure shows that there is a reciprocal relationship between the size of the object and the scattered intensity, decaying significantly up to values of $2\pi/d_x$, where d_x is the size of the object. This means that in order to probe the large-scale structural features that are of interest in the study of soft materials, it is necessary to consider small values of q. When considering the nature of q in Eqn. 2.3, it is clear that such experiments would benefit from small values of θ and large values of λ. Hence, the appication of small angle scattering (SAS).

CODE BLOCK 2.1: An example code block for the Abelès method for the calculation of reflectometry, adapted from Ref. [8].

```python
import numpy as np


def abeles(q_values, sld, d):
    """
    Calculates the reflectometry from a set of layers of a given scattering
    length density.

    Parameters
    ----------
    q_values: float, array-like
        The q-vector values over which the reflectometry is to be calculated.
    sld: float, array-like
        An array of scattering length densities of length N, where N is the
        number of layers present.
    d: float, array-like
        An array of thicknesses of length N, where N is the number of layers
        present.

    Returns
    -------
    float, array-like
        The reflected intensity over the given q-vector values.

    """
    R = np.zeros_like(q_values)
    kn = np.sqrt(q_values[:, np.newaxis] ** 2.0 / 4.0 - 4.0 * np.pi * sld)
    B = np.zeros((2, 2, q_values.size))
    B[0, 0, :] = 1
    B[1, 1, :] = 1
    k = kn[:, 0]
    nmax = sld.size
    for n in range(1, nmax):
        kn1 = kn[:, n]
        r = (k - kn1) / (k + kn1)
        betan = k * d[n]
        if n > 0:
            Mn = np.array(
                [
                    [np.exp(betan * 1j), r * np.exp(betan * 1j)],
                    [r * np.exp(-betan * 1j), np.exp(-betan * 1j)],
                ]
            )
        else:
            Mn = np.array([[1, r], [r, 1]])
        p0 = B[0, 0, :] * Mn[0, 0, :] + B[1, 0, :] * Mn[0, 1, :]
        p1 = B[0, 0, :] * Mn[1, 0, :] + B[1, 0, :] * Mn[1, 1, :]
        B[0, 0, :] = p0
        B[1, 0, :] = p1
        p0 = B[0, 1, :] * Mn[0, 0, :] + B[1, 1, :] * Mn[0, 1, :]
        p1 = B[0, 1, :] * Mn[1, 0, :] + B[1, 1, :] * Mn[1, 1, :]
        B[0, 1, :] = p0
        B[1, 1, :] = p1
        k = kn1
    R = (B[0, 1, :] * np.conj(B[0, 1, :])) / (B[0, 0, :] * np.conj(B[0, 0, :]))
    R[np.where(np.isnan(R))] = 1.0
    return np.real(R)
```
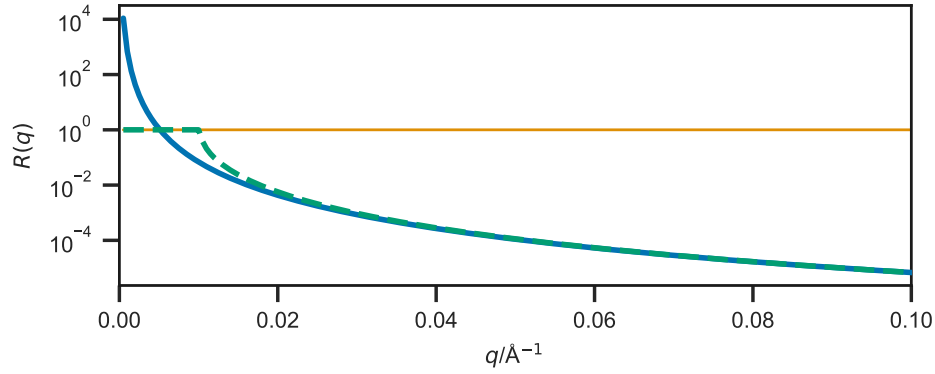
FIGURE 2.9: A comparison of the kinematic approach (blue solid line), and the dynamical approach (green dashed line), to determine the reflected intensity from the material with the scattering length density profile given in Fig. 2.7(a). It is clear that at low q, there is a noticable deviation between the two.
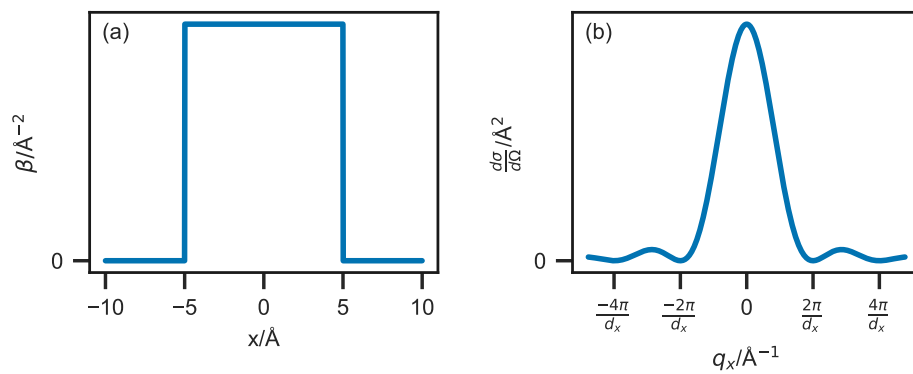

FIGURE 2.10: The effect of a Fourier transform (a) the scattering length density profile for some object with a width of $10\,\text{Å}$, (b) the Fourier transform of this object showing the minima in the differential cross section at values of $2n\pi/10$, where n is some integer.
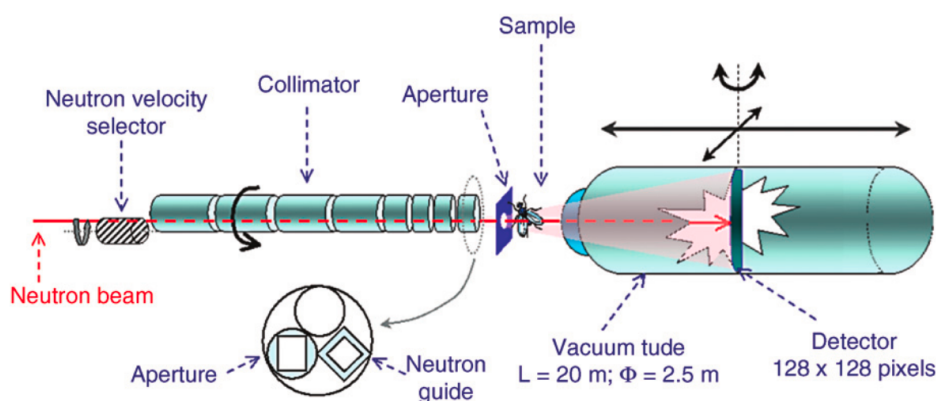
FIGURE 2.11: A schematic of the D22 instrument of the ILL, from Ref. [15]. Reprinted/adapted by permission from Springer Nature Customer Service Centre GmbH: Springer Nature Small-Angle Neutron Scattering and Applications in Soft Condensed Matter by I. Grillo© (2008).

A SAS experiment generally involves some sample being placed in the path of the probing radiation; and the scattering pattern that results from this tranmission is measured at some distance, as is shown in Fig. 2.11 for the D22 SANS instrument of the ILL. SAS instruments are usually very large, due to the large post sample flight path that is necessary to reach the small angles being measured; a longer flight path allows more space for angular divergence. Transmission SAS can provide information about the size, shape and orientation of the sample's components [13]. The range in q that is typically covered by a SAS instrument is usually around $5 \times 10^{-3}\,\text{Å}^{-1}$ to $0.5\,\text{Å}^{-1}$, which corresponds to $10\,\text{Å}$ to $1000\,\text{Å}$ in real-space. The neutron or X-ray detector of a SAS instrument is often two-dimensional, meaning that for an isotropic scattering profile, the detector image is radially averaged to give an $I(q)$ scattering profile. It is possible to increase the q-range of a SAS instrument through the introduction of wide-q detector banks close to the sample or small-q detector banks further away. This allows the SANS2D instrument, at the ISIS Neutron and Muon Source, to have a total range from $2 \times 10^{-3}\,\text{Å}$ to $2\,\text{Å}$ [14].

Analysis

A radially averaged SAS pattern can be considered as consisting of two section that arise from the form and structure factors for the scattering species. The form factor gives information about the average shape of the scattering particle, while the structure factor is a measaure of the interaction present between the objects. It is often possible to control the presence of the structure factor by changing the concentration of the sample, eventually the concentration will be so low that all interparticle interaction is screened by the solvent [16]. This method is frequency applied in BioSAXS applications, where the interactions between the protein molecules are of less interest than the overall structure of the complex. However, with micelles it is not always possible to remove the structure factor, as the critical micelle concentration may be higher than the minimum concentration at which the structure factor is present. It is possible to deconvolvute the structure and form factors for a micellar solution by studying different concentrations, assuming that the form of the micelle is concentration independent.

The rigorous, model-independent method for the analysis of SAS involves taking the inverse Fourier transform of the scattering, to give an auto-correlation functionss of the average particle in the system, which following a deconvolution procedure will resolve the

radially averaged scattering length density profile. However, this is often cumbersome and has a low information density, when compared to model-dependent techniques.

There are two common, and straight-forward analysis procedures that can be used to give an understanding of the scattering species. The first is the Guiner approximation, which is used in the determination of the radius of gyration, R_g, of the scattering species, at "infinite dilution". This scattering law is only valid at very small values of q, where $q < R_g^{-1}$ [3],

$$\ln[I(q)] = \ln[I(0)] - \left(\frac{R_g^2}{3}\right)q^2. \tag{2.35}$$

This relationship allows the radius of gyration to be found by plotting the scattering profile transformed into $\ln[I(q)]$ vs. q^2, and evaluating the gradient at low q. The Guinier plot for the scattering from a sphere with a radius of 20 Å is shown in Fig. 2.12, where the radius of gyration correlates with the radius of the sphere, R, as follows,

$$R_g = \sqrt{\frac{3}{5}}R. \tag{2.36}$$

The Guinier analysis is very common in the study of proteins by SAS, as it allows for the determination of the protein size in the native, solution phase [17]. Another common analysis of SAS data comes in the form of Porod's law, which states that for large values of q, the scattering intensity becomes proportional to Sq^{-4}, where S is the surface area of the sample. This mens that by plotting $I(q)q^4$ vs. q and extrapolating to $q \rightarrow \infty$, it is possible to determine the external surface area of the system [13]. Using the surface area it is then possible to qualitatively determine the 'roughness' of the system.

In the calculation of a SAS pattern, both the structure and form factors will contribute. Therefore, when we model the pattern, the differential cross-section has the following form, when the system is centro-symmetric.

$$\frac{\mathrm{d}\sigma(q)}{\mathrm{d}\Omega} = N_\rho \Delta \rho^2 V_p^2 P(q)S(q), \tag{2.37}$$

where N_ρ is the number density of the particles, $\Delta \rho$ is the difference in scattering length density between the particles and the solvent, V_p is the particle volume, $P(q)$ is the particle form factor, and $S(q)$ is the structure factor [18]. Therefore is it necessary to understand how the function of the form factor and structure factor come about.

The most common method for the modelling of the form-factor is by using very coarse shapes; such as spheres, cylinders, or ellipses. This involves the evaulation of analytical or quasi-analytical solutions for the scattering, which have been derived for many common shapes. The solution for a sphere, was solved in the early 19th century by Lord Rayleigh [18].

$$P(q) = \left\{ \frac{3\{\sin(qR) - qR\cos(qR)\}}{(qR)^3} \right\}^2, \tag{2.38}$$

where R is the radius of the sphere. A comparison between a possible experimental scattering pattern and the scattering generated from Eqn. 2.38 is shown in Fig. 2.13. Analytical form factors exist for a wide variety of shapes; these can be found in software such as SASView and SASFit [19, 20].

The structure factor accounts for the scattering interference that arises from the interaction of different particles. This is modelled using expressions which depend on the nature of the scattering particles; hard-sphere, sticky hard-spheres, screened Coulomb, etc. Structure factor expressions are generated as solutions to the Ornstein-Zernike Eqn. [21]. The most
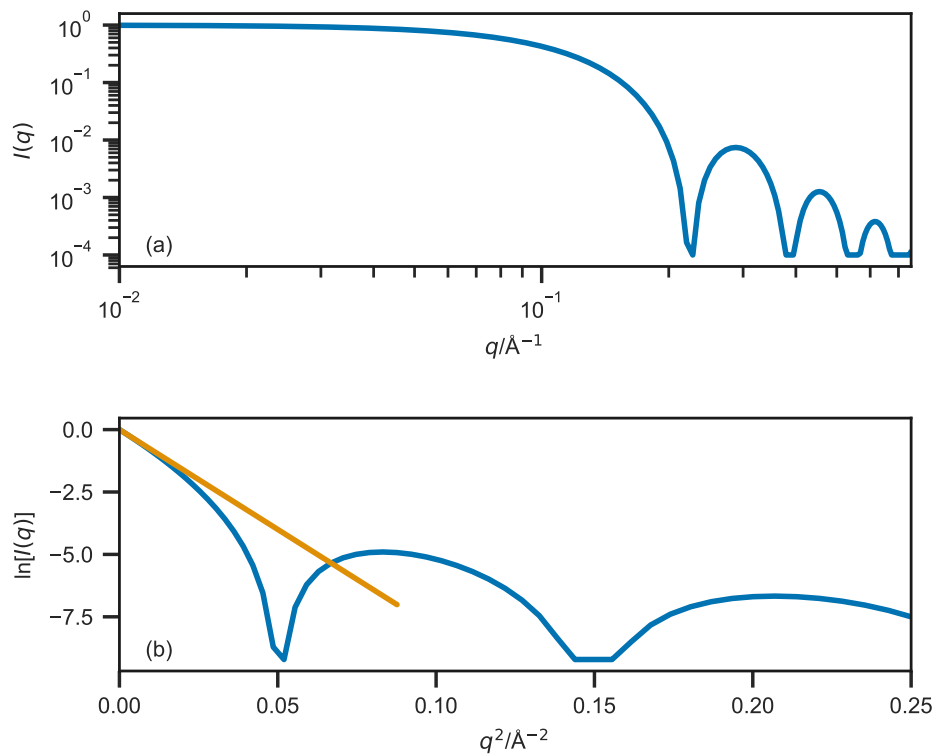
FIGURE 2.12: The Guinier plot, (a) the ideal scattering profile from a sphere of radius $20\,\text{Å}$, (b) the associated Guinier plot, with a straight line (orange) at low-q showing the radius of gyration to be $\sim 15.5\,\text{Å}$.
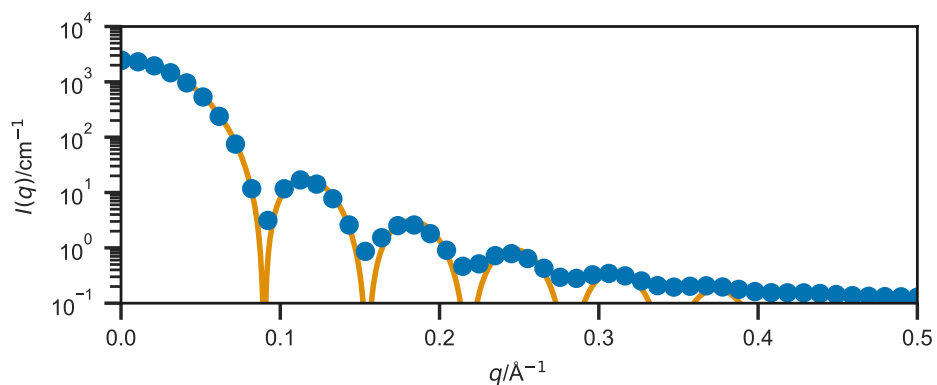

FIGURE 2.13: The SANS profile of a micelle of C_{16}TAB with radius $(50 \pm 3)\,\text{Å}$ (circles, generated using SASView [19], with instrumental smearing) compared with a curve of Eqn. 2.38, where $R = 50\,\text{Å}$ (solid line).

relevant sturcture factor in terms of micelle modelling is probably the Hayter-Penfold [22], this is where the micelles are modelled as like-charged, soft spheres. Again, a whole range of these strucuture factor functions are built into the SASView package [19].

In order to evelute the scattering profile from an atomic, or coarse-grained system, it is possible to use the Deybe equation [23]. This is an analysis relation for the determination of the scattering profile based on the atomic positions, $\mathbf{r}_i$,

$$I(q) = \sum_i^N \sum_j^N b_i b_j \frac{\sin\left(q|\mathbf{r}_i - \mathbf{r}_j|\right)}{q|\mathbf{r}_i - \mathbf{r}_j|}, \tag{2.39}$$

where, N is the number of particles, q is the scattering vector, and b_i and b_j are the scattering lengths of particles i and j respectively, for a coarse-grained particle this can be obtained from summing the scattering lengths of the constituent atoms. The Debye equation is powerful, however it is not intrinsically parellisible and as a result scales as $\mathcal{O}(N^2)$. In order to improve the efficiency of the calculation of the scattering profile, a variety of methods have been developed that offer a sufficiently accurate approximation [24, 25]. The Golden Vector method, developed by Watson and Curtis [25] scales as $\mathcal{O}(Nn)$, where n is the number of scattering vectors used in the calculation. In this method, the scattering amplitude is calculated numerically for a single $\mathbf{q}$-vector,

$$I(\mathbf{q}) = \left[\sum_i^N b_i \cos\left(\mathbf{q} \cdot \mathbf{r}_i\right)\right]^2 + \left[\sum_i^N b_i \sin\left(\mathbf{q} \cdot \mathbf{r}_i\right)\right]^2. \tag{2.40}$$

This is carried out for n scattering vectors that are selected in an orientationally averaged fashion from a quasi-uniform lattice on a sphere. This was first developed such that n is a number from the Fibonacci sequence [24], however for the Golden Vector method, n may be any positive integer. This leads to the scattering vectors being calculated as,

$$\begin{aligned} q_x^{(k)} &= q \cos\left[\sin^{-1}\left(\frac{2k}{n}\right)\right] \cos\left(\frac{2\pi k}{\Phi}\right), \\ q_y^{(k)} &= q \cos\left[\sin^{-1}\left(\frac{2k}{n}\right)\right] \sin\left(\frac{2\pi k}{\Phi}\right), \\ q_z^{(k)} &= \frac{2kq}{n}, \end{aligned} \tag{2.41}$$

where, k runs from $-(n-1)/2, \ldots, 0, \ldots, (n-1)/2$ and Φ is the golden ratio,

$$\Phi = \frac{1 + \sqrt{5}}{2}. \tag{2.42}$$

The approximate orientationally averaged scattering is then found as an average of the scattering from each of ther individual q-vectors,

$$I(q) = \frac{1}{n}\left\{\sum_{k=(1-n)/2}^{(n-1)/2} I[\mathbf{q}^{(k)}]\right\}. \tag{2.43}$$

The accuracy of this calculation increases with n, however good agreement between experiment and simulation has been shown for $n < 100$ even for highly anisotropic systems [25].
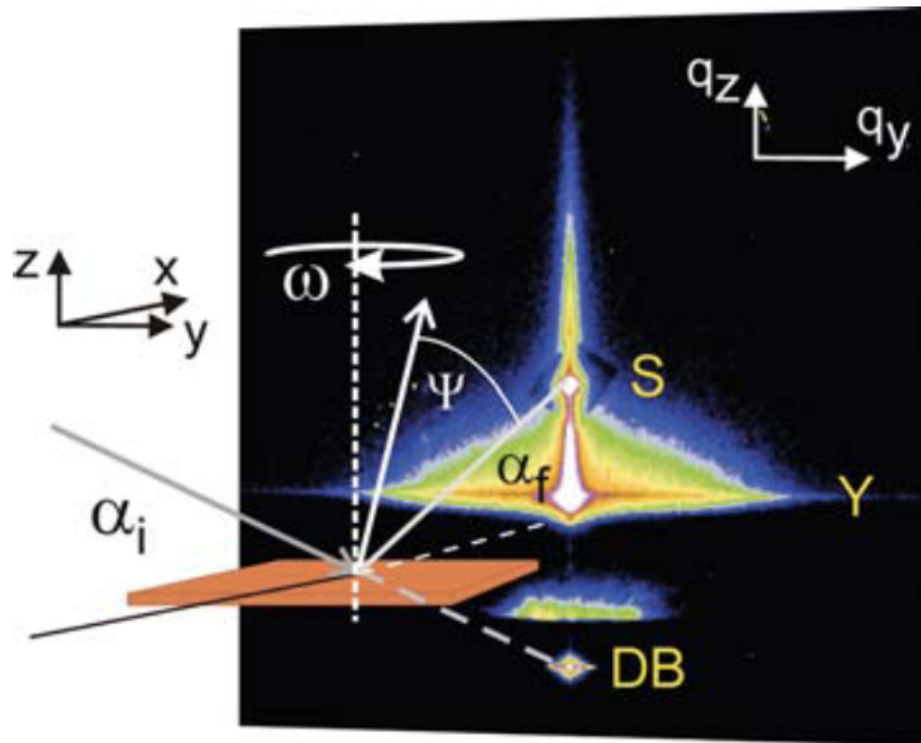
FIGURE 2.14: A schematic of the geometry of a GISAS experiment, where α_i is the incident angle, α_f is the exit angle, and ϕ is the out-of-plane angle, from Ref. [28]. Reprinted/adapted by permission from Springer Nature Customer Service Centre GmbH: Springer Nature A Basic Introduction to Grazing Incidence Small-Angle X-Ray Scattering by P. Müller-Buschbaum$^{©}$ (2009).

2.1.8 Grazing incidence small angle scattering

While reflectometry is the study of specular reflections from a layer structure, grazing incidence small angle scattering (GISAS) is the study of the off-specular reflections, those where the scattering vector has x- and y-components in addition to the z-component. This off-specular scattering is that which arises from the heterogeneity present at the interface. This means that GISAS is ideal for the study of material with nanostructure in the plane of the interface, such as organic semiconducting matierals or polyerm-grafted nanoparticles at an interface [26, 27]. The geometry of a GISAS experiment on a thin film material is shown in Fig. 2.14, which also shows a typical GISAS pattern.

In terms of GISAS instrumentation, it can be consider as an amalgamation of a reflectometry instrument and a small angle scattering instrument. The sample environment is that from a reflectometry instrument, while the two-dimensional detector required is that commonly associated with small angle scattering. Commonly, GISAS is found as an additional capability of another instrument, such as the grazing incidence small angle neutron scattering (GISANS) capability of D22 at the ILL or the GISAS setup at I07 of the Diamond Light Source [29, 30]. However, as GISAS has grown in popularity as a technique, GISAS focused instruments have been installed, such as MiNaXS at DESY in Hamburg and Beamline 7.3.3 at the ALS in San Francisco [31, 32].
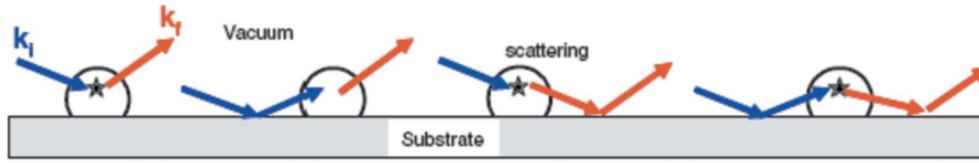
FIGURE 2.15: The four possible way in which some probing radiation may interact
with a sample within the DWBA; scattering, reflection-then-scattering,
scattering-then-reflection, and reflection-then-scattering-then-reflection, from Ref. [33].

Analysis

The analysis process for a GISAS pattern is substanially more complex than for either the
SAS or reflectometry counterparts. This is due to the fact that for SAS, the Born approxima-
tion is conserved, and only a single scattering event is considered. While for reflectometry,
there is a well defined theoretical background that enables the analysis were the Born ap-
proximation is not valid. This is not the case for GISAS, since for off-specular reflectometry
to occur, the probing radiation will undergo both scattering and reflectometry events simul-
taneously. In order to account for this, generally, the distorted wave Born approximation
(DWBA) is envoked. This is an extension of the Born approximation, wherein there are
four possible ways in which the probing radition may interact with the, these are shown in
Fig. 2.15.

One of the most common methods for the analysis of a GISAS pattern is Bragg peak
analysis. This is where Bragg peaks of crystallinity in the GISAS pattern are selected and
analysed in terms of Bragg's and Snell's laws to account for the effects of the surface and
substrate, this allows the dependence of q_z to be determined [34, 35]. While useful, this
analysis approach is limited to systems with high crystallinity, such as stacked lamellae [36].
This method cannot be easily applied to understand less organised arrangements in soft
matter systems, as these give rise to broad, smeared peaks with no clear centre.

Another simplified method for the analysis of a GISAS pattern involves the effective sur-
face approximation. This is where, from the two-dimensional GISAS pattern, selected cuts
are taken and analysed only as a function of q_y. This can be used to probe depth dependent
properties, as taking such a cut effectively considered the lateral structure at a given depth,
rather than the both the lateral structure and that normal to the interface. For incident an-
gles $\alpha_i \gg \alpha_c$ and at constant q_z, the scattering intensity in the DWBA simplifies and the
differential cross section is given by [37],

$$\frac{\mathrm{d}\sigma}{\mathrm{d}\Omega} = \frac{A\pi^2}{\lambda^4}\big[(1-n^2)T_iT_f\big]^2 F(\mathbf{q}), \qquad (2.44)$$

where A is the iluminated surface area, $T_{i,f}$ are the Fresnel transmission factors for incidence
and reflectance, and $F(\mathbf{q})$ is the diffuse-scattering factors, which are dependent on the form
and structure factors of the lateral structure.

Currently there exists a handful of software packages that are designed to aid in the
structural analysis by GISAS. These include, but are not limited to, IsGISAXS, BornAgain,
and HipGISAXS [38–40]. These software packages generally impliment analytical solutions
to the DWBA by considering different form and structure factors for some system. In order
to have some understanding of the structure that should be fitted to the experimental data,
it is often necessary to perform electron microscopy measurements to educate the analysis
process.

2.2 Probing radiation

This work is focussed on the use of X-ray and neutron scattering, therefore it is pertinent to discuss how each of these probing radiation is produced and detail the advantages of each with resepect to the other.

2.2.1 Generation of X-rays

X-rays are a form of electromagnetic radiation similar to visible light, albeit with a much shorter wavelength, from $0.01\,\mathrm{nm}$ to $10\,\mathrm{nm}$. There are three common ways to produce X-rays; two are available within the laboratory, while the other is exclusive to large scale facilities.

The two laboratory source X-ray generation techniques are the X-ray tube and the rotating anode. An X-ray tube consists of a filament and an anode within a vacuum chamber, by passing a high voltage electrical current across the filament electrons are emitted which accelerate towards the anode. On collision with the anode, the rapid deceleration results in the emission of X-rays of a characteristic wavelength based on the anode material [41]. The most common material for an X-ray tube anode is copper which gives off radiation of about $8\,\mathrm{keV}$.

The other common laboratory method for the generation of X-rays is the rotating anode, which is an improvment on the X-ray tube. In the X-ray tube, each time that an electron contacts the anode there is some energy transfer, this means that over many millions of collisions, the temperature of the anode can raise significantly, leading to a temperature limitation on the X-ray flux available. This lead to the development of the rotating anode, this is simply where the anode is made from a rotating wheel, so that the bombardment is spread across the whole wheel reducing the energy localisation. This allows an increase in the photon flux by about an order of magnitude [41].

The third method of X-ray generation is at a synchrotron facility, this method has the drawback that it requires access to a national or international faciliy; such as Diamond Light Source (DLS) or the European Synchrotron Radiation Facility (ESRF). The way in which X-rays are generated at the synchrotron involves the acceleration of an electron, rather than the deceleration as with the laboratory sources. This is achieved by having relativistic electrons travel in around a curve, from Newtonian mechanics it is known that travelling on a curve at constant speed is equivalent to acceleration. This is achieved by firstly accelerating the electrons, produced in an linear accelerator (Linac), to near the speed of light in a booster synchrotron before injecting them into the storage ring. In the storage ring, the electrons are kept at relativistic speeds with bending magnets (BM) and straight sections making up a ring (Fig. 2.16). The circularity of the ring is dependent on the number of bending magnets that make up the ring; for example, DLS has 48 bending magnets with 48 straight sections.

When an electron accelerates (or travels on a curve), Cherenkov radiation is emitted in accordance with the Cherenkov relation,

$$n_i \beta_c \cos \theta_e = 1, \tag{2.45}$$

where, n_i is the refractive index for the dielectric medium, β_c is the fraction of the speed of light at which that electron is travelling, and θ_e is the angle between the electron trajectory and the trajectory of the resulting photon [42]. The curve is the result of a bending magnet, meaning that at each bending magnet there can be a beamline which gives out synchrotron light. The light this is given off from a bending magnet is continuous and broad, covering a wide range of the electromagnetic spectrum. The alternative to a bending magnet beamline is a beamline which is served by an insertion device (ID). An insertion device is able to
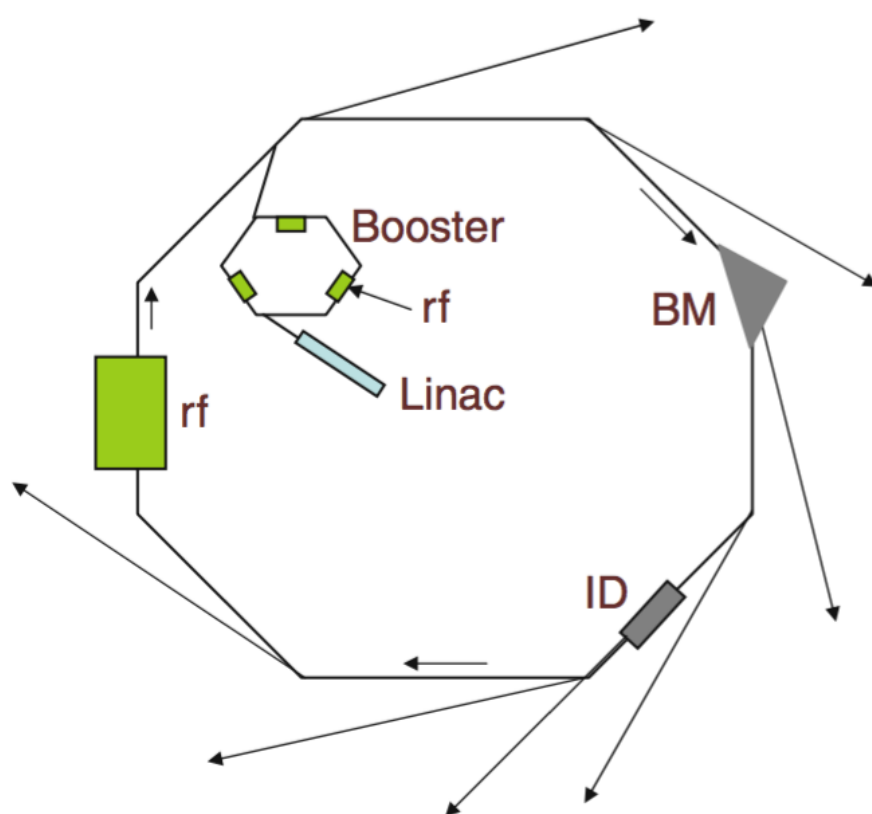
FIGURE 2.16: A schematic representation of a synchrotron radiation source, identifying the Linac, the booster ring, the radio-frequency cavities (rf), the bending magnet (BM) and the insertion device (ID), from Ref. [42]. Reprinted/adapted by permission from Springer Nature Customer Service Centre GmbH: Springer Nature Bases of Synchrotron Radiation, Light Sources, and Features of X- Ray Scattering Beamlines by M.C. García-Gutiérrez, D.R. Rueda© (2009).
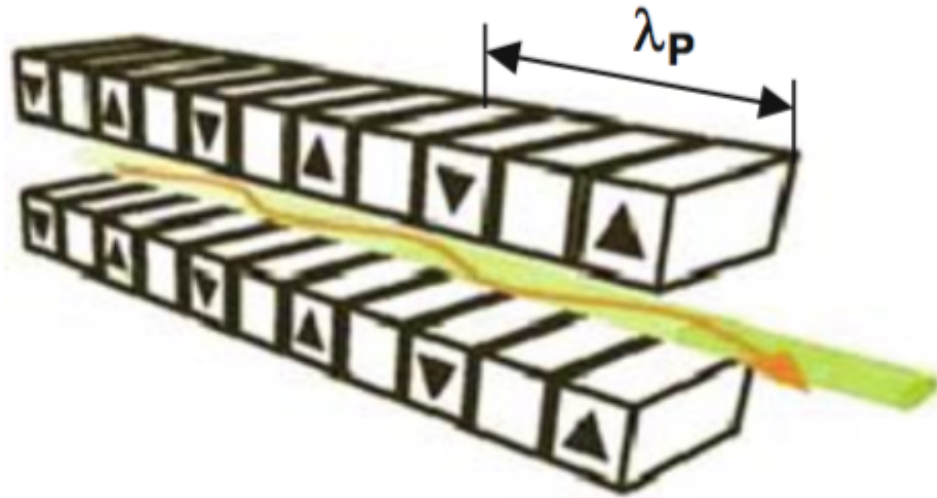
FIGURE 2.17: A diagram of an undulator insertion device such as that on I07 or I22 where λ_P is the period length between opposing magnets, from Ref. [42]. Reprinted/adapted by permission from Springer Nature Customer Service Centre GmbH: Springer Nature Bases of Synchrotron Radiation, Light Sources, and Features of X- Ray Scattering Beamlines by M.C. García-Gutiérrez, D.R. Rueda© (2009).

TABLE 2.1: A comparision of the photon brilliance from different light sources. Adapted, with permission of Oxford University Press©, from Ref. [3].

Light source	Approximate brilliance/ $\mathrm{photons\,s^{-1}mrad^{-2}0.1\%bandwidth^{-1}}$
Candle	10^5
X-ray tube	10^8
Sun	10^{10}
Bending magnet	10^{15}
Undulator	10^{20}

offer more specific radiation characteristics (photon energy, narrower band) than a bending magnet, and are placed on the magnet-free straight sections of the synchrotron. Common insertion devices include wavelength shifters, wigglers, and undulators.

The type of insertion device that is present at both I07 and I22 at DLS is an undulator. An undulator consists of a series of magnets of opposing polarity whihc causes the electrons to 'wiggle' back and forth (Fig. 2.17). This results in a superposition of radition from N_P sources, where N_P si the number of magnets, yielding quasi-monochromatic radiation. The brilliance of different X-ray sources are compared in Table 2.1, this shows the significant benefit that an undulator offers in terms of photon brilliance.

2.2.2 Generation of neutrons

Neutrons hold an advantage over X-rays, particularly for application to the study of soft matter, in the ability to utilise contrast variation to increase the quantity of information from the sample, this is discussed in deatil in Section 2.2.3. However, neutrons cannot be produced safely on a laboratory scale, therefore it is always necessary to visit large scale facilities to harness neutrons for scattering experiments. These facilities come in two flavours;

the reactor source and the spallation source, each offering unique benefits.

Neutron reactor sources, such as the Institut Laue-Langevin (ILL) in Grenoble, France, as currently the most common format of neutron source and are capable of producing the highest average neutron flux, the number of neutrons per second per unit area, for example the High-Flux Reactor at the ILL is capable of producing a neutron flux of 1.5×10^{15} neutrons $s^{-1} cm^{-2}$ [43]. A reactor source operates on the principle of nuclear fission, where an atomic nucleus is capable of breaking down into smaller nuclei, overcoming the strong nuclear force. This often involves using uranium enriched with its fissile isotope, ^{235}U, which after the initial absorption of a stray neutron, from a cosmic ray, or spontaneous fission, will undergo fission to release, on average, 2.5 daughter neutrons, an example of a possible uranium fission mechanism is:

$$n + {}^{235}U \longrightarrow {}^{236}U \longrightarrow {}^{134}Xe + {}^{100}Sr + 2\,n.$$
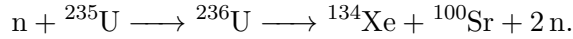
This type of mechanism is the basis for research, and nuclear power, reactors [3]. One of the major drawbacks for reactor neutron sources is the percieved public opinion towards such facilities. Major saftey concerns, such as "nuclear meltdown" and the resulting nuclear waste, mean that reactor souces are often unpopular and therefore struggle to obtain funding required for operation.

The other form of neutron source is a spallation source, this is much less controversial as it does not require fissile materials and hence there is no risk of a nuclear disaster. The ISIS neutron and muon source (Oxfordshire, UK) is an example of a spallation source, where high energy protons, $800\,MeV$ [44], are accelerated towards a tungsten target. When the protons strike the target, they can cause the release of a series of neutrons, the first batch of neutrons are given off with too high an energy to be useful, however, less excited neutrons are given off by secondary emissions. In addition to the public preception benefit, spallation sources also have a technological advantage in the time-of-flight technique. The time-of-flight (ToF) technique is based on the fact that at a spallation source, it is possible to know the time at which the neutron was ejected by the target to a high level of precision and accuracy, and therefore it is possible to measure the time taken for the neutron to reach the instrument. Since the neutron is a particle of a finite mass, m, it is possible to correlate the velocity, v, of the particle with the kinetic energy, E_k,

$$E_k = \frac{mv^2}{2}, \tag{2.46}$$

and with knowledge of the energy of the particle, its wavelength λ, can be determined by the de Broglie relation,

$$E = h\omega = \frac{hv}{\lambda}, \tag{2.47}$$

where, h is Planck's constant and ω is the neutron frequency. Therefore, the wavelength of the neutron is proportional to the inverse of the particle's velocity, and hece the time-of-flight, t_F,

$$\lambda = \frac{h}{mv} = \frac{ht_F}{mL_F}, \tag{2.48}$$

where, L_F is the distance between the target and the instrument. The fact that the neutrons can spread out in the flight from the target means that wavelength-dispersive techniques, where the neutron wavelength is measured rather than the scattering angle, are possible at spallation sources which cannot be carried out at reactor sources. The negative side-effect of current spallation sources is that they have a lower average flux than reactor sources, however the building of the European Spallation Source (ESS) will change this as it offers an average flux similar to that of a reactor source, but with the benefits of the spallation

technique.

A problem that is inherent for both reactor and spallation sources is that the energy of the neutrons given off is usually too high to be used to study condensed materials, such as soft matter. This means that moderation must be used to reduce the energy of the neutrons passing through the sample. The neutrons which are considered to be optimal for the study of condensed materials are thermal neutrons, named because their energy is approximately that of ambient temperature. Thermal neutrons are achieved by allowing the neutrons to pass through a large volume of moderator material, usually graphite or heavy water (D_2O), stored at $300\,K$ before they reach the instrument [3].

2.2.3 Contrast variation

The scattering profile generated by the interaction of some system with radiation depends on three factors:

- the spatial arrangement of the atoms in the system,

- the instrument being used to measure the pattern; instrumental resolution function, and

- the interaction between the radiation and the matter under investigation.

This final factor is perhaps better known as the 'scattering contrast', this is an extremely important factor in the study of soft matter, particularly when the probing radiation is the neutron. The scattering contrast makes it possible to select individual components of the system and investigate their structural properties [45]. The differential cross-section, $\mathrm{d}\sigma/\mathrm{d}\Omega$ of a point scatterer, as shown in Eqn. 2.15, varies only with respect to the scattering length of the species, b,

$$\frac{\mathrm{d}\sigma}{\mathrm{d}\Omega} \propto b^2. \tag{2.49}$$

However, as discussed in Section 2.1.4, it is often easier to use the scattering length density, ρ.

When an X-ray interacts with an atom, it is scattered by the interaction with the electrons, this is due to the X-ray being a form of electromagnetic radiation. Furthermore, it means that the scattering length of an atom by an X-ray is directly proportional to the number of electrons in the atom, so it is therefore difficult to discern between the scattering from a carbon atom (6 electrons) and a nitrogen atom (7 electrons), furthermore the scattering from hydrogen atoms is practically non-existent.

The scattering length a neutron by an atom varies unsystematically with respect to the atomic number of a species, this is shown in Fig. 2.18. Furthermore to the apparently random variation with changes in atomic number, there is also significant variation with mass number, e.g. between isotopes of the same atom. This is also dependance due to the magnetic state of the atom, however this is normally unimportant for soft matter. The scattering lengths differ with the nuclear spin energy level, this leads to an average scattering length, $\langle b \rangle$, for isotopes where the nuclear spin is non-zero ($S \neq 0$). There are two forms of scattering, coherent and incoherent, for which the scattering cross-sections, σ, are determined by,

$$\begin{aligned} \sigma_{\mathrm{coh}} &= 4\pi\langle b \rangle^2 \\ \sigma_{\mathrm{incoh}} &= 4\pi(\langle b^2 \rangle - \langle b \rangle^2) \end{aligned} \tag{2.50}$$

The coherent scattering is the scattering from nuclei that all have the same value of $\langle b \rangle$, and leads to the important scattering pattern. Whereas, the incoherent scattering is caused by the 'disorder' between the isotopes, and is the cause of the background present in the
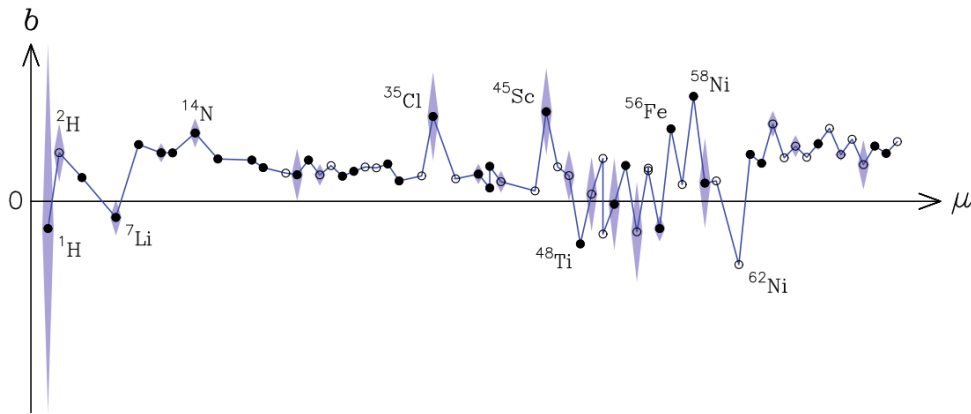
FIGURE 2.18: The variation of the average neutron scatteirng length, $\langle b \rangle$ (circles), with atomic mass, μ. The standard deviation, Δb, is indicated with the shaded regions. Reproduced, with permission of Oxford University Press$^{©}$, from Ref. [3].

TABLE 2.2: Examples of coherent and incoherent scattering cross-sections, from Ref. [45].

Isotope	S	$\sigma_{coh}/10^{-28}$ m	$\sigma_{incoh}/10^{-28}$ m
^{1}H	$1/2$	1.8	79.7
^{2}H	1	5.6	2.0
^{12}C	0	5.6	–
^{14}N	1	11.6	0.3
^{16}O	0	4.2	–

measurement. Examples of these scattering cross-sections for nuclei relevant to soft matter are shown in Table 2.2. It can be seen that the incoherent scattering from the ^{1}H nuclei is more than forty times the coherent scattering. This leads to a large, intrusive background present in the scattering pattern of hydrogenous samples. The difference between the scattering of ^{1}H and ^{2}H, evident in Table 2.2, can lead to a very useful technique if soft matter scattering, known as contrast variation. The idea of contrast variation is based on the substitution of one isotope of an atom for another, while not introducing significant change to the properties of the material. Traditionally the benefit of this came in terms of contrast matching out a part of the system to reduce the dimensionality of the problem for analysis. For example, by matching the solvent scattering length density to that of the tails of the surfactants at the centre of a micelle there would only be scattering from the heads, and conversely there would only be scattering from the tails if the solvent had the same scattering length density as the head groups. This means that the problem becomes more straightforward as there are fewer variable parameters when fitting the data. This idea is represented graphically in Fig. 2.19. The technique of contrast variation may also be used in terms of data analysis. By increasing the number of data sets corresponding to a single model at different constrasts, the solution for the true structure of the model from the scattering data becomes more robust. This is due to the fact that each different contrast can be considered as an independent measurement of the same system, and hence each set of scattering data can be used within the data analysis procedure to obtain the best global agreement to the experiment. This co-refinement of multiple experiments can, under the right conditions, be used to simultenously consider both neutron and X-ray datasets [9].

There is also the possibility of using contrast variation when the probing radiation is
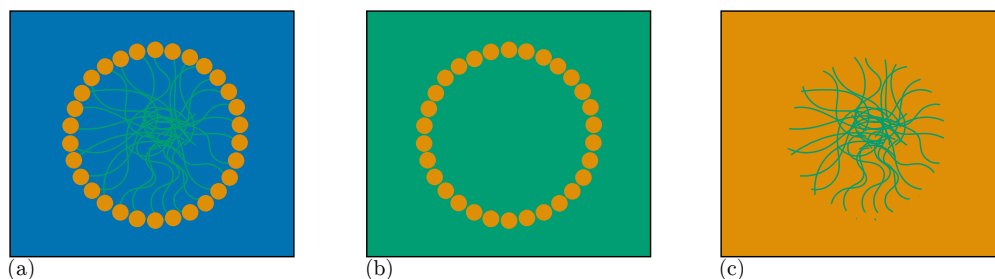
FIGURE 2.19: The effect of varying the scattering length density of the solvent in a micelle system, (a) the system in pure solvent, (b) the solvent is contrast matched to the surfactant tails, and (c) the solvent is contrast matched to the surfactant heads.

the X-ray, through the use of anomalous scattering. This is where different wavelengths of radiation give different scattering, when the wavelengths are on opposite sides on an X-ray absorption edge. This is not frequenctly used for soft matter species, as the X-ray absorption edges for elements common in soft matter (H, C, N, O, etc.) are at very low X-ray energies so generally outside of the accessible range [45].

2.3 Classical simulation

In order to simulation a real chemical system, it is necessary to model the electrons of the molecules and their interactions. This is usually achieved using quantum mechanical calculations, where the energy of the system is calculated by finding som approximate solution to the Schrödinger equation. However, quantum mechanical calculations are very computationally expensive, and are realistically limited to hundreds of atoms. In order to simulate a soft matter system such as a lipid monolayer or polymer nanoparticles, it is necessary to simply the calculation being performed. This leads to classical simulation, where mathematical functions are used to determined the potential energy of the system. Classical simulations is used substantially in this work, in terms of both molecular dynamics simulations and energy minimisation methods (see Section 2.4). Therefore, it is necessary to introduce the underlying theory on which this method is defined.

2.3.1 Potential models

Potential modelling is a more computationally efficient method for the calcution of the potential energy of a chemical system. A potential model consists of a series of mathematical functions that depend on the atomic positions, $\mathbf{r}$. Each of the functions represents the potential energy of a different interaction for a given atom. Broadly, these interactions can be split into bonded and non-bonded, such that the total energy may be described as follows,

$$E_{\text{total}}(\mathbf{r}) = E_{\text{bonded}}(\mathbf{r}) + E_{\text{non-bonded}}(\mathbf{r}) \tag{2.51}$$

The total potential energy is then the sum of the potential energy for each of the individual atoms.

The bonded terms are used to describe different aspects of chemical bonds. These typically consist of bond stretchs, angle bends and dihedral torsions; within the OPLS2005 potential model [46], these interactions have the following mathematical form,

$$
\begin{aligned}
E_{\text{bonded}}(b, \theta, \phi) = &\sum_{\text{bonds}} K_b (b - b_0)^2 + \sum_{\text{angles}} K_\theta (\theta - \theta_0)^2 \\
&+ \sum_{\text{dihedrals}} \frac{1}{2} \{ A_1 [1 + \cos(\phi)] + A_2 (1 - \cos(2\phi)) + A_3 (1 + \cos(3\phi)) \},
\end{aligned}
\tag{2.52}
$$

where, K_b and b_0, K_θ, θ_0, and A_1, A_2, and A_3 are potential model dependent parameters for the bonds, angles, and dihedrals respectively, while b, θ, and ϕ are the bond lengths, the size of the angles, and the size of the dihedrals that depend on the atom positions. It can be seen that both the bond stretch and angle bend have harmonic functions, whereas the dihedral consists of a more complex multiple cosine function. The values of the potential model dependent parameters are determined as outlined in Section 2.3.2.

The non-bonded terms are a series of functions that describe the potential energy of intermolecular interactions, such as eletrostatics and London dispersion forces. The potential energy of the short-range interactions are usually modelled as a combination of the attractive London dispersion interaction and the repulsive exchange forces that arise from the Pauli exclusions principle [47]. These often forms such as shown below for the Lennard-Jones potential model [48],

$$
E_{\text{non-boned}}(r) = E_{\text{repulsive}} + E_{\text{attractive}} = \frac{A}{r^{12}} - \frac{B}{r^6} = 4\varepsilon \left[\left(\frac{\sigma}{r} \right)^{12} - \left(\frac{\sigma}{r} \right)^6 \right]
\tag{2.53}
$$

where, r is the distance between two particles, A and B are potential model dependent parameters, and σ and ϵ are simple reformations of these parameters,

$$
A = 4\varepsilon\sigma^{12} \quad B = 4\varepsilon\sigma^6.
\tag{2.54}
$$

Fig. 2.20 shows each component of the Lennard-Jones potential model for atoms of argon, using parameters for A and B determined by Rahman [49]. The Lennard-Jones is not the only potential model that may be used for the modelling of the short-range non-bonded interactions, others such as the Buckingham and Morse potentials exist [50, 51]. However, the Lennard-Jones model has been used heavily in this work.

While the short-range interactions are accounted for by a function such as the Lennard-Jones potential model, the potential energy of the long-range electrostatic interactions are usually modelled, more consistently, using Coulomb's law for classical electrostatic interaction between point particles [52, 53],

$$
E_{\text{Coulomb}}(r) = \frac{1}{4\pi\varepsilon_0} \frac{q_i q_j e^2}{r^2},
\tag{2.55}
$$

where, r is the distance between the two particles, ε_0 is the dielectric permittivity of the vacuum, e is the charge of the electron, and q_i and q_j are the electronic charges on each of the particles. It is clear that when q_i and q_j have the opposite signs Coulomb's law is always attractive.

An example of a very large classical simulation would be ~ 3 million atoms [54]. However, this is still only 1.8×10^{-16} mol which is not remotely realistic as a simulation of a *real* system. A common method to allow for the apparent simulation of a much larger system is the use of periodic boundary conditions. This is where a boundary condition is applied
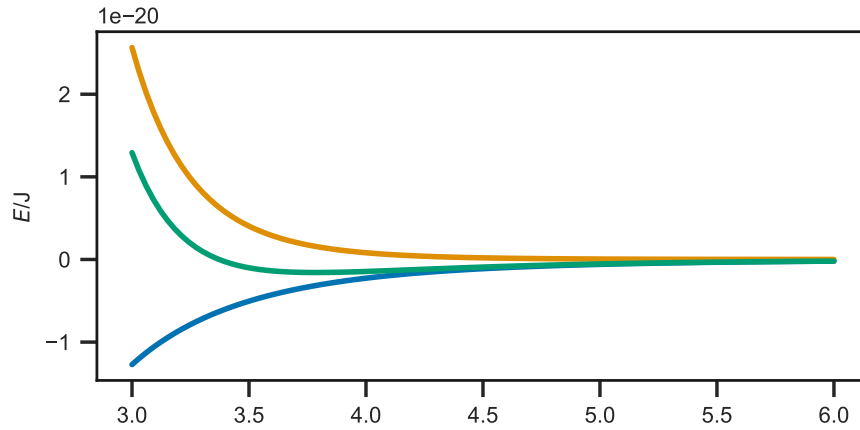
FIGURE 2.20: The form of each component; attractive (blue), repulsive (orange), of the Lennard-Jones potential model (green) for argon, using parameters from Rahman [49].
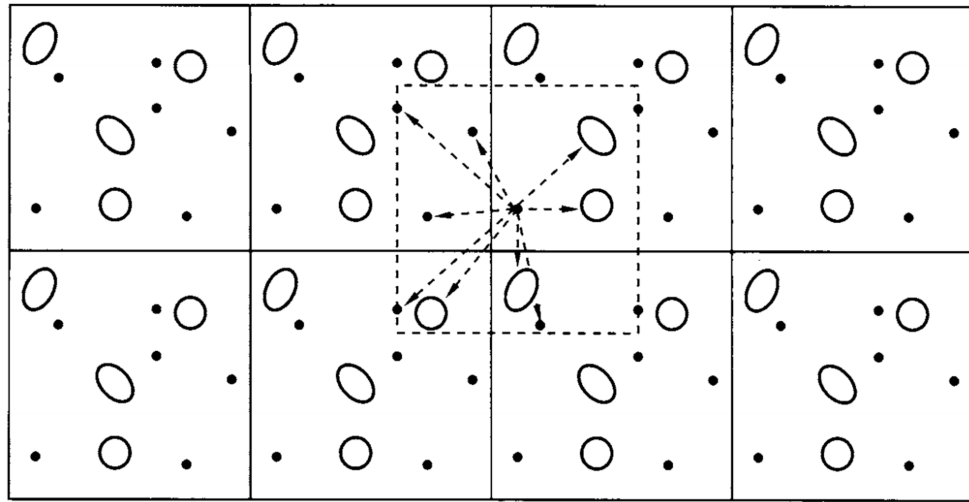
FIGURE 2.21: A graphical representation of the periodic boundary conditions. Reprinted by permission from Elsevier© from Ref. [55].

to the edges of the simulation cell, such as to mimic an infinite system, assuming that the simulation cell is surrounded by identical images of itself (Fig. 2.21). Using the periodic boundary condition means that atomic diffusion is conserved as when an atom reaches the edge of the simulation cell, it will apear on the other side such that it came from the adjacent periodic time. The use of a periodic boundary condition is particularly powerful in the simulation of homogenous systems, such as liquids. However, periodicity may result in unexpected results for particular systems, as is discussed in Chapter 4.

The periodic boundary condition leads to the necessity to consider another important factor from classical simulation. This is the cut-off, the distance after which the energy between to particles is considered to be zero. The cut-off is an important component of simulation that must be considered, as if there was no energy cut-off distance it would be possible for multiple counting of particle-particle interactions to occur. This multiple counting would arise from counting between particles in different periodic images that have already been accounted for elsewhere. As a result, the energy cut-off distance should always be less than half the shortest simulation cell vector. An additional benefit of the energy cut-off distance is that is means that it is not necessary to calculate the energy between every particle, as once

CODE BLOCK 2.2: An example of some code that may be used to
generate the Lennard-Jones energy for a given atomistic system, which
accounts for the periodic boundary condition and the energy cut-off
distance.

```python
import numpy as np


def lj_energy(coordinates, cell, cut_off, A, B):
    """
    Calculates the potential energy arising from the Lennard-Jones potential
    model from a series of atomistic particles.

    Parameters
    ----------
    coordinates: float, array-like (N, 3)
        An array of the x, y, and z coordinates for each of the N particles in
        the simulation.
    cell: float, array-like
        An array of length 3 containing the simulation cell vectors.
    cut_off: float
        The potential energy cut_off value for the simulation.
    A: float
        The A parameter in the Lennard-Jones potential model.
    B: float
        The B parameter in the Lennard-Jones potential model.

    Returns
    -------
    float, array-like
        An array of length N containing the energy of each particle in the
        simulation.
    """
    energy = np.zeros((coordinates.shape[0]))
    for i in range(coordinates.shape[0] - 1):
        for j in range(i + 1, coordinates.shape[0]):
            d = positions[j] - positions[i]
            d = d % cell
            r = np.sqrt(np.sum(np.squared(d)))
            if r > cut_off:
                break
            else:
                energy[i] += A / np.power(r, 12) - B / np.power(r, 6)
                energy[j] += A / np.power(r, 12) - B / np.power(r, 6)
    return energy
```

the distance has been found to be greater then the cut-off distance the energy for this interaction is immediately taken as zero, increasing computational efficiency. Code Block 2.2 gives an example of some code that could be used to calculate the Lennard-Jones energy of an atomistic system, where both the periodic boundary condition and the energy cut-off distance are considered.

TALK ABOUT THE EWALD SUMMATION.

2.3.2   Parameterisation

2.3.3   Coarse-graining

2.4   Simulation methods

2.4.1   Energy minimisation

2.4.2   Molecular dynamics

2.5   Optimisation techniques

2.5.1   Markov-chain Monte Carlo

2.5.2   Particle Swarm

3 Chemically consistant modelling of X-ray and neutron reflectometry

4 Applying atomistic and coarse-grained simulation to neutron reflectometry analysis

5 Assessing the applicability of particle swarm methods to fitting coarse-grained small angle scattering data

6 Parameterisation of accurate forcefields for the analysis of GISAS data

7 Developing open-source teaching resources for classical simulation and scattering

8 Conclusions

List of Figures

List of Tables

List of Code Blocks

Bibliography

[1] V. García Sakai and A. Arbe, *Curr. Opin. Colloid Interface Sci*, 2009, **14**, 381–390, DOI: 10.1016/j.cocis.2009.04.002.

[2] B. Farago, *Curr. Opin. Colloid Interface Sci*, 2009, **14**, 391–395, DOI: 10.1016/j.cocis.2009.07.004.

[3] D. S. Sivia, *Elementary Scattering Theory*, Oxford University Press, Oxford, UK, 2011.

[4] A. R. McCluskey and K. J. Edler, *Curr. Org. Chem.*, 2018, **22**, 750–757, DOI: 10.2174/1875692115666170612104439.

[5] F. Abelès, *Ann. Phys.*, 1948, **12**, 504–520, DOI: 10.1051/anphys/194812030504.

[6] L. G. Parratt, *Phys. Rev.*, 1954, **95**, 359–369, DOI: 10.1103/PhysRev.95.359.

[7] F. Foglia, M. J. Lawrence and D. J. Barlow, *Curr. Opin. Colloid Interface Sci.*, 2015, **20**, 235–243, DOI: 10.1016/j.cocis.2015.08.001.

[8] A. Nelson, S. Prescott, I. Gresham and A. R. McCluskey, *refnx v0.0.17*, 2018, DOI: 10.5281/zenodo.1327191.

[9] A. Nelson, *J. Appl. Crystallogr.*, 2006, **39**, 273–276, DOI: 10.1107/S0021889806005073.

[10] *RasCAL*, https://sourceforge.net/projects/rscl/, Accessed: 2016-08-08.

[11] Y. Gerelli, *J. Appl. Crystallogr.*, 2016, **49**, 330–339, DOI: 10.1107/S1600576716000108.

[12] Y. Gerelli, *J. Appl. Crystallogr.*, 2016, **49**, 712, DOI: 10.1107/S1600576716002466.

[13] B. T. M. Willis and C. J. Carlile, *Experimental Neutron Scattering*, Oxford University Press, Oxford, UK, 2009.

[14] *ISIS – SANS2D*, https://www.isis.stfc.ac.uk/Pages/Sans2d.aspx, Accessed: 2018-09-25.

[15] I. Grillo, in *Soft Matter Characterization*, ed. R. Borsali and R. Pecora, Springer, Dordrecht, Dordrecht, The Netherlands, 1st edn., 2008, ch. 13, pp. 723–782, DOI: 10.1007/978-1-4020-4465-6_13.

[16] K. J. Edler and D. T. Bowron, *Curr. Opin. Colloid Interface Sci.*, 2015, **20**, 227–234, DOI: 10.1016/j.cocis.2015.07.002.

[17] S. Skou, R. E. Gillilan and N. Ando, *Nat. Protoc.*, 2014, **9**, 1727–1739, DOI: 10.1038/nprot.2014.116.

[18] J. S. Pedersen, in *Neutrons, X-rays and Light: Scattering Methods Applied to Soft Condensed Matter*, ed. P. Linder and T. Zemb, Elsevier, Amsterdam, The Netherlands, 1st edn., 2002, ch. 14, pp. 381–390.

[19] *SASView*, https://www.sasview.org/, Accessed: 2018-11-11.

[20] *SASfit*, https://kur.web.psi.ch/sans1/SANSSoft/sasfit.html, Accessed: 2018-11-11.

[21] R. Kelin, in *Neutrons, X-rays and Light: Scattering Methods Applied to Soft Condensed Matter*, ed. P. Linder and T. Zemb, Elsevier, Amsterdam, The Netherlands, 1st edn., 2002, ch. 13, pp. 351–380.

[22] J. B. Hayter and J. Penfold, *Mol. Phys.*, 1981, **42**, 109–118, DOI: 10.1080/00268978100100091.

[23] D. P. J. W., *Ann. Phys.*, 1915, **351**, 809–823, DOI: 10.1002/andp.19153510606.

[24] S. D. I., *Acta. Crsyt.*, 1994, **A50**, 391–402, DOI: 10.1107/S0108767393013492.

[25] W. M. C. and C. J. E., *J. Appl. Crystallogr.*, 2013, **46**, 1171–1177, DOI: 10.1107/S002188981301666X.

[26] P. Müller-Buschbaum, S. V. Roth, M. Burghammer, E. Bauer, S. Pfister, C. David and C. Riekel, *Physica B Condens. Matter*, 2005, **357**, 148–151, DOI: 10.1016/j.physb.2004.11.045.

[27] H. Zhang, W. Wang, S. Mallapragada, A. Travesset and D. Vaknin, *J. Phys. Chem. C*, 2017, **121**, 15424–15429, DOI: 10.1021/acs.jpcc.7b02549.

[28] P. Müller-Buschbaum, in *Applications of Synchrotron Light to Scattering and Diffraction in Materials and Life Sciences*, ed. T. A. Ezquerra, M. C. Garcia-Gutierrez, A. Nogales and M. Gomez, Springer-Verlag, Berlin, Germany, 2009, ch. 3, pp. 61–89, DOI: 10.1007/978-3-540-95968-7.

[29] P. Müller-Buschbaum, J. S. Gutmann, R. Cubitt and W. Petry, *Physica B Condens. Matter*, 2004, **350**, 207–210, DOI: 10.1016/j.physb.2004.04.028.

[30] C. Nicklin, T. Arnold, a. J. Rawle and A. Warne, *J. Synchrotron Rad.*, 2016, **23**, 1245–1253, DOI: 10.1107/S1600577516009875.

[31] A. Buffet, A. Rothkirch, R. Döhrmann, V. Körstgens, M. M. Abul Kashem, J. Perlich, G. Herzog, M. Schwartzkopf, R. Gehrke, P. Müller-Buschbaum and S. V. Roth, *J. Synchrotron Rad.*, 2012, **19**, 647–653, DOI: 10.1107/S0909049512016895.

[32] A. Hexemer, W. Bras, J. Glossinger, E. Schaible, E. Gann, R. Kirian, A. MacDowell, M. Church, B. Rude and H. Padmore, *J. Phys. Conf. Ser.*, 2010, **247**, 012007, DOI: 10.1088/1742-6596/247/1/012007.

[33] A. Hexemer, and P. Müller-Buschbaum, *IUCrJ*, 2015, **2**, 106–125, DOI: 10.1107/S2052252514024178.

[34] B. Lee, I. Park, H. Park, C.-T. Lo, T. Chang and R. E. Winans, *J. Appl. Crystallogr.*, 2007, **40**, 496–504, DOI: 10.1107/S0021889807011399.

[35] P. Busch, M. Rauscher, D.-M. Smilgies, D. Posselt and C. M. Papadakis, *J. Appl. Crystallogr.*, 2006, **39**, 433–442, DOI: 10.1107/S0021889806012337.

[36] P. Busch, D. Posselt, D.-M. Smilgies, M. Rauscher and C. M. Papadakis, *Macromolecules*, 2007, **40**, 630–640, DOI: 10.1021/ma061695c.

[37] A. Naudon, D. Babonneau, D. Thiaudière and S. Lequien, *Physica B Condens. Matter*, 2000, **283**, 69–74, DOI: 10.1016/S0921-4526(99)01894-3.

[38] R. Lazzari, *J. Appl. Crystallogr.*, 2002, **35**, 406–421, DOI: 10.1107/S0021889802006088.

[39] J. Burle, C. Durniak, J. M. Fisher, M. Ganeva, G. Pospelov, W. Van Herck, J. Wuttke and D. Yurov, *BornAgain – Software for simulating and fitting X-ray and neutron small-angle scattering at grazing incidence (www.bornagainproject.org)*, 2018.

[40] S. T. Chourou, A. Sarje, X. S. Li, E. R. Chan and A. Hexemer, *J. Appl. Crystallogr.*, 2013, **46**, 1781–1795, DOI: 10.1107/S0021889813025843.

[41] H. Schnablegger and Y. Singh, *The SAXS Guide: Getting acquainted with the principles*, Anton Paar GmbH., Graz, Austria, 4th edn., 2017.

[42] M. C. Garcìa-Gutièrrez and D. R. Rueda, in *Applications of Synchrotron Light to Scattering and Diffraction in Materials and Life Sciences*, ed. T. A. Ezquerra, M. C. Garcìa-Gutièrrez, A. Nogales and M. Gomez, Springer-Verlag Berlin Heidelberg, Heidelberg, Germany, 1st edn., 2009, vol. 776, ch. 1, pp. 1–20, DOI: 10.1007/978-3-540-95968-7.

[43] *ILL::Neutrons for Science::Technical characteristics*, `https://www.ill.eu/reactor-environment-safety/high-flux-reactor/technical-characteristics/`, Accessed: 2016-08-08.

[44] *ISIS – How ISIS works*, `https://www.isis.stfc.ac.uk/Pages/What-does-ISIS-Neutron-Muon-Source-do.aspx`, Accessed: 2018-09-25.

[45] P. Schurtenberger, in *Neutrons, X-rays and Light: Scattering Methods Applied to Soft Condensed Matter*, ed. P. Linder and T. Zemb, Elsevier, Amsterdam, The Netherlands, 1st edn., 2002, ch. 7, pp. 145–170.

[46] B. J. L., H. S. Beard, Y. Cao, A. E. Cho, W. Damm, R. Farid, A. K. Felts, T. A. Halgren, D. T. Mainz, J. R. Maple, R. Murphy, M. P. Philipp, D. M. Repasky, L. Y. Zhang, B. J. Berne, R. A. Friesner, E. Gallicchio and R. M. Levy, *J. Comp. Chem.*, 2005, **26**, 1752–1780, DOI: 10.1002/jcc.20292.

[47] A. R. Leach, *Molecular modelling: principles and applications*, Addison Wesley London Ltd., Harlow, UK, 1st edn., 1996.

[48] J. E. Lennard-Jones, *Proc. R. Soc. Lond. A*, 1924, **106**, 463–477, DOI: 10.1098/rspa.1924.0082.

[49] A. Rahman, *Phys. Rev.*, 1964, **136**, A405–A411, DOI: 10.1103/PhysRev.136.A405.

[50] R. A. Buckingham, *Proc. R. Soc. Lond. A*, 1938, **168**, 264–283, DOI: 10.1098/Frspa.1938.0173.

[51] P. M. Morse, *Phys. Rev.*, 1929, **34**, 57–64, DOI: 10.1103/PhysRev.34.57.

[52] C. A. Coulomb, *Histoire de l'Académie Royale des Scienes*, 1788, **Imperimerie Royale**, 569–577.

[53] C. A. Coulomb, *Histoire de l'Académie Royale des Scienes*, 1788, **Imperimerie Royale**, 577–611.

[54] J. Gumbart, L. G. Trabuco, E. Schreiner, E. Villa and K. Schulten, *Structure*, 2009, **17**, 1453–1464, DOI: 10.1016/j.str.2009.09.010.

[55] D. Frenkel and B. Smit, *Understanding Molecular Simulation: From Algorithms to Applications*, Academic Press, San Diego, USA, 1st edn., 1996.